

Early Planet Formation in Embedded Disks (eDisk) III: A first high-resolution view of sub-mm continuum and molecular line emission toward the Class 0 protostar L1527 IRS

MEREL L.R. VAN 'T HOFF,¹ JOHN J. TOBIN,² ZHI-YUN LI,³ NAGAYOSHI OHASHI,⁴ JES K. JØRGENSEN,⁵
ZHE-YU DANIEL LIN,³ YURI AIKAWA,⁶ YUSUKE ASO,⁷ ITZIAR DE GREGORIO-MONSALVO,⁸ SACHA GAVINO,⁵ ILSEUNG HAN,^{9,7}
PATRICK M. KOCH,⁴ WOJIN KWON,^{10,11} CHANG WON LEE,^{9,7} JEONG-EUN LEE,¹² LESLIE W. LOONEY,¹³
SUCHITRA NARAYANAN,¹⁴ ADELE PLUNKETT,² JINSHI SAI (INSA CHOI),⁴ ALEJANDRO SANTAMARÍA-MIRANDA,⁸
RAJEEB SHARMA,⁵ PATRICK D. SHEEHAN,² SHIGEHISA TAKAKUWA,^{15,4} TRAVIS J. THIEME,^{16,17,18} JONATHAN P. WILLIAMS,¹⁴
SHIH-PING LAI,^{16,17,18,4} NGUYEN THI PHUONG,^{19,20} AND HSI-WEI YEN⁴

¹*Department of Astronomy, University of Michigan, 1085 S. University Ave., Ann Arbor, MI 48109-1107, USA*

²*National Radio Astronomy Observatory, 520 Edgemont Rd., Charlottesville, VA 22903 USA*

³*Department of Astronomy, University of Virginia, 530 McCormick Rd., Charlottesville, VA 22904, USA*

⁴*Academia Sinica Institute of Astronomy & Astrophysics, 11F of Astronomy-Mathematics Building, AS/NTU, No.1, Sec. 4, Roosevelt Rd, Taipei 10617, Taiwan, R.O.C.*

⁵*Niels Bohr Institute, University of Copenhagen, Øster Voldgade 5–7, 1350, Copenhagen K, Denmark*

⁶*Department of Astronomy, Graduate School of Science, The University of Tokyo, 7-3-1 Hongo, Bunkyo-ku, Tokyo 113-0033, Japan*

⁷*Korea Astronomy and Space Science Institute, 776 Daedeok-daero, Yuseong-gu, Daejeon 34055, Republic of Korea*

⁸*European Southern Observatory, Alonso de Cordova 3107, Casilla 19, Vitacura, Santiago, Chile*

⁹*Division of Astronomy and Space Science, University of Science and Technology, 217 Gajeong-ro, Yuseong-gu, Daejeon 34113, Republic of Korea*

¹⁰*Department of Earth Science Education, Seoul National University, 1 Gwanak-ro, Gwanak-gu, Seoul 08826, Republic of Korea*

¹¹*SNU Astronomy Research Center, Seoul National University, 1 Gwanak-ro, Gwanak-gu, Seoul 08826, Republic of Korea*

¹²*Department of Physics and Astronomy, Seoul National University, 1 Gwanak-ro, Gwanak-gu, Seoul 08826, Korea*

¹³*Department of Astronomy, University of Illinois, 1002 West Green St, Urbana, IL 61801, USA*

¹⁴*Institute for Astronomy, University of Hawai'i at Mānoa, 2680 Woodlawn Dr., Honolulu, HI 96822, USA*

¹⁵*Department of Physics and Astronomy, Graduate School of Science and Engineering, Kagoshima University, 1-21-35 Korimoto, Kagoshima, Kagoshima 890-0065, Japan*

¹⁶*Institute of Astronomy, National Tsing Hua University, No. 101, Section 2, Kuang-Fu Road, Hsinchu 30013, Taiwan*

¹⁷*Center for Informatics and Computation in Astronomy, National Tsing Hua University, No. 101, Section 2, Kuang-Fu Road, Hsinchu 30013, Taiwan*

¹⁸*Department of Physics, National Tsing Hua University, No. 101, Section 2, Kuang-Fu Road, Hsinchu 30013, Taiwan*

¹⁹*Korea Astronomy and Space Science Institute, 776 Daedeok-daero, Yuseong-gu, Daejeon 34055, Republic of Korea*

²⁰*Department of Astrophysics, Vietnam National Space Center, Vietnam Academy of Science and Technology, 18 Hoang Quoc Viet, Cau Giay, Hanoi, Vietnam*

ABSTRACT

Studying the physical and chemical conditions of young embedded disks is crucial to constrain the initial conditions for planet formation. Here, we present Atacama Large Millimeter/submillimeter Array (ALMA) observations of dust continuum at $\sim 0''.06$ (8 au) resolution and molecular line emission at $\sim 0''.17$ (24 au) resolution toward the Class 0 protostar L1527 IRS from the Large Program eDisk (Early Planet Formation in Embedded Disks). The continuum emission is smooth without substructures, but asymmetric along both the major and minor axes of the disk as previously observed. The detected lines of ^{12}CO , ^{13}CO , C^{18}O , H_2CO , $\text{c-C}_3\text{H}_2$, SO , SiO , and DCN trace different components of the protostellar system, with a disk wind potentially visible in ^{12}CO . The ^{13}CO brightness temperature and the H_2CO line ratio confirm that the disk is too warm for CO freeze out, with the snowline located at ~ 350 au in the envelope. Both molecules show potential evidence of a temperature increase around the disk-envelope interface. SO seems to originate predominantly

in UV-irradiated regions such as the disk surface and the outflow cavity walls rather than at the disk–envelope interface as previously suggested. Finally, the continuum asymmetry along the minor axis is consistent with the inclination derived from the large-scale (100'' or 14,000 au) outflow, but opposite to that based on the molecular jet and envelope emission, suggesting a misalignment in the system. Overall, these results highlight the importance of observing multiple molecular species in multiple transitions to characterize the physical and chemical environment of young disks.

1. INTRODUCTION

Planets form in disks around young stars, starting with the growth of dust grains beyond interstellar medium sizes. Evidence for planet formation already being underway when the disk is still embedded in its natal envelope has been inferred from low dust opacity spectral indexes in Class 0 sources (Kwon et al. 2009; Shirley et al. 2011), dust polarization (e.g., Kataoka et al. 2015, 2016; Yang et al. 2016), decreasing dust masses derived from (sub-)millimeter observations for more evolved systems (e.g., Williams et al. 2019; Tychoniec et al. 2020), and the lack of CO isotopologue emission toward the protostellar position due to grain growth in the Class I system TMC1A (Harsono et al. 2018). In addition, rings in continuum emission, which could be a signpost of forming planets (e.g., Bryden et al. 1999; Zhu et al. 2014; Dong et al. 2018), are observed in disks as young as only ~ 0.5 Myr (ALMA Partnership et al. 2015; Segura-Cox et al. 2020; Sheehan et al. 2020). Characterizing the physical and chemical conditions in young disks is thus crucial in understanding disk evolution and planet formation.

L1527 IRS (also known as IRAS 04368+2557) is the first Class 0 source toward which a Keplerian rotating disk was established (Tobin et al. 2012). This low-mass protostar is located in the L1527 dark cloud in the Taurus star-forming region and has been observed extensively from the near-infrared to centimeter wavelengths. Based on Gaia Data Release 2 (DR2), Luhman (2018) measured a distance of 139–141 pc for L1527, consistent with the analysis of Gaia DR2 and very long baseline interferometry (VLBI) data by Galli et al. (2019). Roccatagliata et al. (2020) group L1527 into the much larger Taurus B region with an average distance of 131.0 ± 1.0 pc, but sources in L1527 have parallaxes closer to the lower end of the range for Taurus B (~ 6.95 mas, corresponding to 143.9 pc). We therefore adopt a distance of 140 pc, which is also consistent with the distance used in earlier works by Kenyon et al. (1994) and Zucker et al. (2019).

L1527 IRS (hereafter L1527) is often classified as a borderline Class 0/I object, as classification is challenging due to the edge-on orientation. Its bolometric temperature and submillimeter luminosity to bolometric luminosity ratio are typical of a Class 0 source, but at a

lower inclination it would be classified as a Class I object (Tobin et al. 2008). The large envelope mass and extended outflow cavities suggest that L1527 is younger than typical Class I sources, but it lacks the collimated outflow of typical Class 0 sources (see e.g., the discussion in Tobin et al. 2013). Recent re-analysis of the spectral energy distribution (SED) classified L1527 as a Class 0 source with a bolometric luminosity of $1.3 L_{\odot}$ and a bolometric temperature of 41 K (Ohashi et al. 2022a).

Single-dish sub-millimeter observations of L1527 have identified a bipolar outflow in ^{12}CO emission with an orientation almost perfectly in the plane of the sky (Tamura et al. 1996; Hogerheijde et al. 1998). Bright bipolar scattered light nebulae extending $\sim 10,000$ au along the east–west outflow axis are visible in infrared observations with the Spitzer Space Telescope and ground-based telescopes (Tobin et al. 2008, 2010), as well as in the recently released JWST NIRCам image (release id 2022-055, PI: K. Pontoppidan¹). The eastern outflow lobe harbors a compact ($\sim 1''$ long) radio continuum jet close to the protostellar position at centimeter wavelengths (Reipurth et al. 2004).

Ohashi et al. (1997) identified a flattened infalling and rotating envelope with a radius of 2000 au from $6''$ resolution C^{18}O observations. The presence of a rotationally supported disk was initially inferred from ^{13}CO observations with the Combined Array for Millimeter-wave Astronomy (CARMA; Tobin et al. 2012) that also resolved the continuum at $0''.35$ resolution, and was later confirmed by observations with the Atacama Large Millimeter/sub-millimeter Array (ALMA; Ohashi et al. 2014; Aso et al. 2017). High-resolution ($0''.15$) continuum observations with ALMA have suggested that the disk is warped with the inner and outer disk boundary between 40 and 60 au (Sakai et al. 2019). Even higher resolution ($0''.08$) observations with the Karl G. Jansky Very Large Array (VLA) initially revealed clumpy substructures in Q -band (Nakatani et al. 2020), but these structures were not confirmed in later observations with higher sensitivity (Sheehan et al. 2022).

Molecular line observations have shown that the disk is warm ($\gtrsim 20$ K), based on the presence of CO gas out

¹ <https://webbtelescope.org/contents/news-releases/2022/news-2022-055>

Table 1. Overview of molecular lines.

Species	Transition	Frequency (GHz)	E_{up}^a (K)	A_{ij}^b (s^{-1})	Δv^c (km s^{-1})	RMS ^d (mJy beam^{-1})	Velocity range ^e (km s^{-1})
^{12}CO	2–1	230.538000	16.6	6.910×10^{-7}	0.635	0.95	–11.30 – –1.13, 0.77 – 9.04
^{13}CO	2–1	220.398684	15.9	5.066×10^{-7}	0.167	1.96	–4.38 – –0.21, 0.46 – 3.97
C^{18}O	2–1	219.560354	15.8	6.011×10^{-7}	0.167	1.49	–3.55 – 3.64
DCN	3–2	217.238538	20.9	4.575×10^{-4}	1.340	0.55	–3.84 – 1.53 ^g
SO	6 ₅ –5 ₄	219.949442	35.0	1.335×10^{-4}	0.167	1.78	–4.05 – 3.30
SiO	5–4	217.104980	31.3	5.196×10^{-4}	1.340	0.58	–13.45 – 1.30
H_2CO	3 _{0,3} –2 _{0,2}	218.222192	21.0	2.818×10^{-4}	1.340	0.51	–3.84 – 2.87
H_2CO	3 _{2,1} –2 _{2,0}	218.760066	68.1	1.577×10^{-4}	0.167	1.42	–3.05 – 3.14
H_2CO	3 _{2,2} –2 _{2,1}	218.475632	68.1	1.571×10^{-4}	1.340	0.48	–2.50 – 2.87
c-C ₃ H ₂	6 _{0,6} –5 _{1,5} ^f	217.822148	38.6	5.396×10^{-4}	1.340	0.54	–1.16 – 1.53
c-C ₃ H ₂	6 _{1,6} –5 _{0,5} ^f	217.822148	38.6	5.396×10^{-4}	1.340	0.54	–1.16 – 1.53
c-C ₃ H ₂	5 _{1,4} –4 _{2,3}	217.940046	35.4	4.026×10^{-4}	1.340	0.52	–1.16 – 1.53
c-C ₃ H ₂	5 _{2,4} –4 _{1,3}	218.160456	35.4	4.041×10^{-4}	1.340	0.50	–1.16 – 1.53
CH ₃ OH	4 ₂ –3 ₁ , E	218.440063	45.6	4.686×10^{-5}	1.340	0.49	–

^a Energy of the transition’s upper level.

^b Einstein A coefficient of the transition.

^c Velocity resolution of the observations.

^d RMS level per channel in the data cubes imaged with a robust parameter of 2.0, measured within a $10''$ region over five empty channels.

^e Velocity range over which emission is detected ($> 3\sigma$) with the system velocity of 5.9 km s^{-1} shifted to 0 km s^{-1} (Caselli et al. 2002; Tobin et al. 2011).

^f These two transitions are blended.

^g DCN is only detected at the 3–4 σ level.

to at least 75 au (van ’t Hoff et al. 2018). The water snowline is suggested to be located between ~ 2 –4 au (van ’t Hoff et al. 2022), but only a tentative detection of a complex molecule (methanol, CH₃OH) in the inner disk has been reported (Sakai et al. 2014a; van ’t Hoff et al. 2020). Observations by Sakai et al. (2014a,b) reveal different morphologies and kinematics for several molecular species, suggesting that they trace different components of the protostellar system. In particular, SO seems to be enhanced in a ring at the disk-envelope interface (see also Ohashi et al. 2014).

While L1527 has been studied at high resolution at multiple wavelengths in continuum emission ($0''.045$ at cm wavelengths and $0''.08$ at mm wavelengths; Sheehan et al. 2022; Ohashi et al. 2022b, respectively), molecular line observations have been limited to a resolution of ~ 0.3 – $0''.5$. Here, we present high angular resolution 1.3 mm continuum ($0''.06$) and molecular line images ($0''.17$) obtained with the ALMA Large Program eDisk (Early Planet Formation in Embedded Disks). The molecular lines detected toward L1527 are ^{12}CO , ^{13}CO , C^{18}O , H_2CO , c-C₃H₂, SO, SiO and DCN. A notable non-detection is CH₃OH. The observations are described in Sect. 2. The structure of the 1.3 mm continuum is presented in Sect. 3.1 and the morphology and spatial origin of the molecular lines in Sect. 3.2. The system’s inclination is discussed in Sect. 4.1, a dynamical estimate of the central mass is made in Sect. 4.2, and the tempera-

ture structure is described in Sect. 4.3. In Sect. 4.4 we discuss the physical and chemical reasons behind the different molecular distributions. Finally, our conclusions are summarized in Sect. 5.

2. OBSERVATIONS

L1527 has been observed as part of the ALMA Large Program eDisk (2019.1.00261.L; PI N. Ohashi) on 14 and 15 October 2022, sampling baselines between 91 and 11,469 m. Observations in a more compact configuration with the purpose of recovering larger spatial scales were carried out through a DDT program (2019.A.00034.S; PI J. Tobin) on 3 December 2021, 16 December 2021 and 3 July 2022. These observations used baselines between 15 and 2617 m. The correlator setup for both programs is centered around $\sim 225 \text{ GHz}$ (1.3 mm) and includes 2 low spectral resolution windows at 976.56 kHz (1.34 km s^{-1}) resolution, 1 spectral window at 488.28 kHz (0.635 km s^{-1}) resolution, and 4 higher spectral resolution windows at 122.07 kHz (0.167 km s^{-1}) resolution. More details about the observations are provided by Ohashi et al. (subm.), and an overview of the molecular lines discussed in this paper is provided in Table 1.

Standard calibration of the data was done using the ALMA Pipeline and a script developed for the eDisk Large Program, as described in Ohashi et al. (subm.) was used for subsequent data reduction and imaging. In short, the continuum emission peaks of all execution blocks were first aligned to a common phase center after

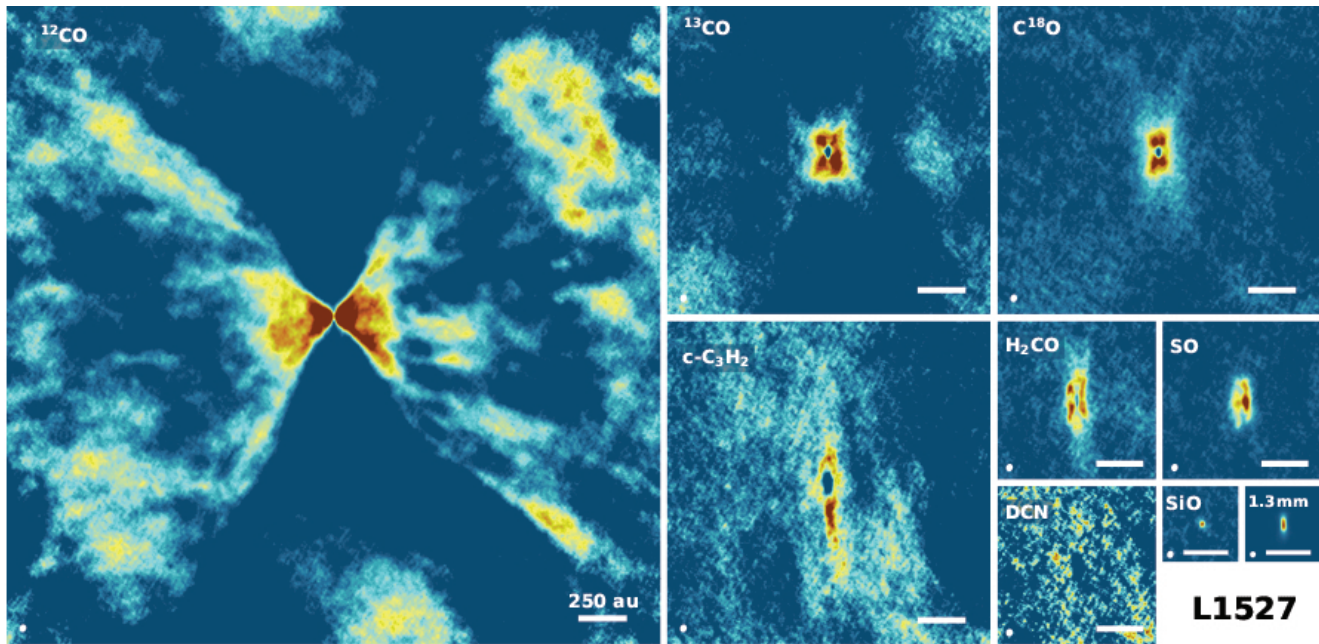


Figure 1. Overview of 1.3 mm continuum and line observations (integrated intensity maps) toward L1527. For H_2CO the $3_{0,3} - 2_{0,2}$ transition is shown, and for $\text{c-C}_3\text{H}_2$ the blended $6_{0,6} - 5_{1,5}$ and $6_{1,6} - 5_{0,5}$ transitions are shown. The images are centered on the source position (R.A. = 04:39:53.9, Dec. = +26:03:09.4). The spatial scale is the same in each panel, with the white scale bar denoting 250 au. The size of the ^{12}CO image is $24'' \times 24''$. All color scales are linear, start at zero, and are saturated to highlight weaker, more extended emission. Intensity scales are shown in Fig. 3. All images are made with a robust parameter of 2.0, and the beam size is depicted in the lower left corner of each panel.

which an amplitude rescaling was applied to the shifted visibilities. The amplitude calibration uncertainty is expected to be $\sim 5\text{--}10\%$. Two rounds of continuum self-calibration were then performed on the aggregate continuum data, first on the short-baseline data only and then on the short- and long-baseline data combined. For L1527, phase and amplitude self-calibration were performed on the short baseline data, while only phase self-calibration was used for the combined data set. The final gain tables were also applied to the line data.

The standard eDisk image products were created with `tclean` using a range of robust parameters (-2.0 , -1.0 , -0.5 , 0.0 , 0.5 , 1.0 and 2.0) for the continuum and robust = 0.5 for the line images. For L1527, line images were also created with a robust value of 2.0 to increase the signal-to-noise ratio, and those images are presented here. The resulting beam size for the line images is approximately $0''.17 \times 0''.14$ (PA = -20°), and the noise levels for the different line cubes are listed in Table 1. Unless noted otherwise, we present the continuum image created with a robust value of -0.5 as a compromise between resolution and sensitivity. This image has a resolution of $0''.056 \times 0''.029$ (PA = 9.3°), and an rms of $29 \mu\text{Jy beam}^{-1}$. The full range of continuum images is presented in Fig. A1. An overview of the continuum and

molecular line observations toward L1527 is presented in Fig. 1.

3. RESULTS

3.1. Continuum

The 1.3 mm continuum image of L1527 obtained with a robust parameter of -0.5 is shown in Fig. 2, and a gallery of images made with different robust parameters is presented in Fig. A1. The continuum image displays an edge-on disk with the major axis along the north-south direction, as previously observed (e.g., Ohashi et al. 1997; Loiseau et al. 2002; Tobin et al. 2008, 2010, 2012, 2013; Sakai et al. 2014b; Aso et al. 2017; Nakatani et al. 2020; Ohashi et al. 2022b; Sheehan et al. 2022). The flared nature of the disk inferred by radiative transfer modeling of multi-wavelength continuum emission (Tobin et al. 2013) is now clearly visible at this high resolution. The emission extends out to a radius of $\sim 0''.5$ (70 au) along the major axis, and in the east-west direction to $\sim 0''.1$ (14 au) above the midplane near the source position and up to $\sim 0''.2$ (28 au) at a radial offset of $\sim 0''.3$ (42 au). Fainter emission extending out to a radius of $\sim 1''$ (140 au) and to $\sim 0''.5$ (70 au) above the midplane is visible in the image obtained with a robust parameter of 2.0. This is most likely due to more faint envelope emission being picked up by the higher sensitiv-

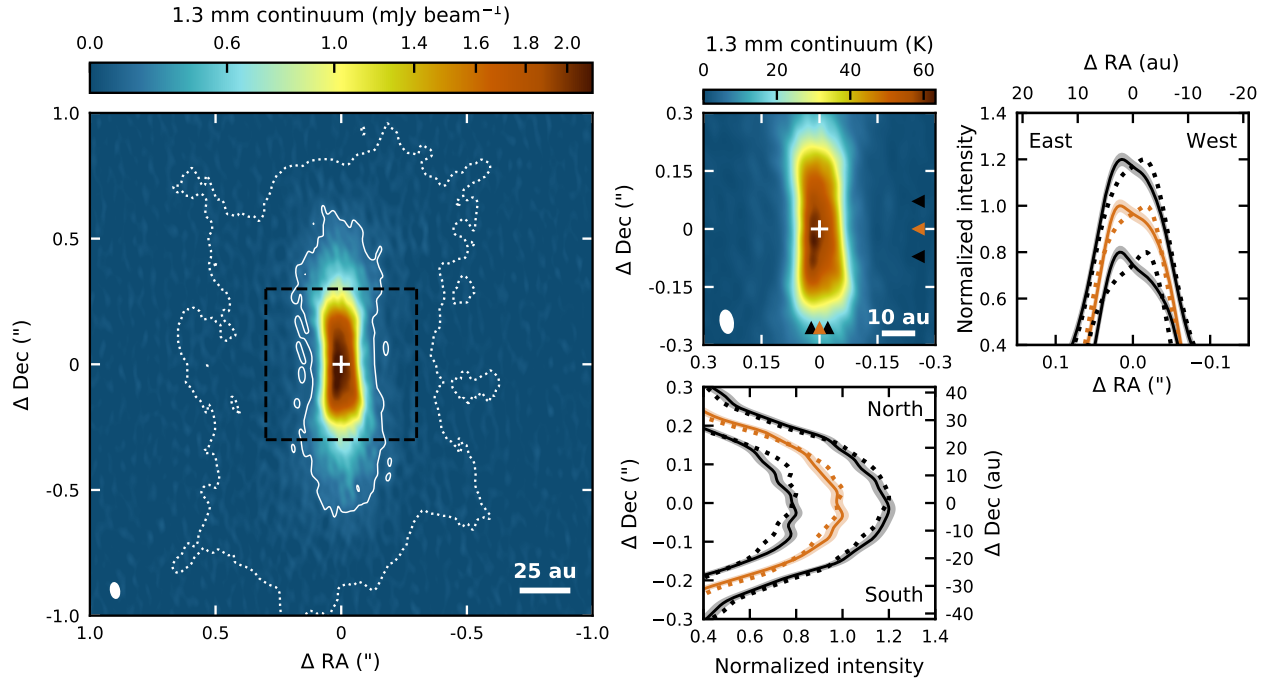


Figure 2. ALMA 1.3 mm continuum image of L1527. The left panel shows the full extent of the continuum imaged with a robust parameter of -0.5 (color scale; beam size of $0''.056 \times 0''.029$, PA = 9.3°), with the solid white contour marking the 5σ level ($0.15 \text{ mJy beam}^{-1}$). The dotted white contour marks the 5σ level ($0.11 \text{ mJy beam}^{-1}$) of the map imaged with a robust parameter of 2.0 (beam size of $0''.123 \times 0''.111$, PA = -13.7°). The white cross marks the source position derived from a Gaussian fit in the image plane (R.A. = $04:39:53.9$, Dec. = $+26:03:09.4$). The black dashed square shows the region depicted in the top middle panel, where the brightness temperature of the continuum is displayed. The top right panel shows the normalized intensity along the disk minor axis at source position (orange curve) and at 10 au to the north (top black curve) and south (bottom black curve). The bottom right panel shows the normalized intensity along the disk major axis at source position (orange curve) and at 3 au to the east (left black curve) and west (right black curve). Black and orange triangles in the continuum image (top middle panel) mark the locations of the intensity profiles. The black curves are shifted by 0.2 in intensity scale with respect to the orange curves for better visibility. The shaded region depicts the 3σ level and the dotted lines are the mirror images of the solid lines to highlight the asymmetries.

ity of the robust = 2.0 image, because the vertical extent of the bright central region is not much more extended (Fig. A1). The brightness temperature for the majority of the disk is 40–60 K (for a robust parameter of -0.5), suggesting that the continuum may be optically thick.

The continuum emission appears smooth with no sign of substructures. However, an asymmetry between the north and south side, with the south side being brighter than the north side, is visible for all robust parameters (see radial cuts for a robust value of -0.5 in Fig. 2). At the highest resolutions (robust values ≤ 0.0 or beam sizes of $0''.062 \times 0''.038$ and smaller), an asymmetry between the east and west side becomes also clear, with the east side being brighter than the west side. The north–south asymmetry is then also more pronounced in the east. The east–west asymmetry is stronger in the south but visible along the entire major axis. The difference in maximum brightness temperature between the southeast and the northeast or southwest is about 10 K.

Because of the flared nature of the disk, a simple 2D Gaussian fit does not represent the emission morphology and total flux density. Therefore, we sum over all pixels with values $> 3\sigma$, which yields a flux density of $192.57 \pm 0.05 \text{ mJy}$ (compared to $139.04 \pm 0.73 \text{ mJy}$ from the Gaussian fit). This is only 9% higher than the 1.3 mm flux reported by Aso et al. (2017) obtained within a $4'' \times 4''$ box from $0''.47 \times 0''.37$ resolution observations. Using a similar aperture, we obtain a slightly lower flux density of 188.78 mJy , which is within 7% of the previously reported value.

For isothermal and optically thin emission, the continuum flux density, S_ν , can be converted into a dust mass using

$$M_{\text{dust}} = \frac{D^2 S_\nu}{\kappa_\nu B_\nu(T_{\text{dust}})}, \quad (1)$$

where D is the distance (140 pc), κ_ν the dust opacity at the observed frequency, and $B_\nu(T_{\text{dust}})$ the Planck function at the observed frequency for a dust temperature of T_{dust} . We adopt a dust opacity of $2.3 \text{ cm}^2 \text{ g}^{-1}$ at the ob-

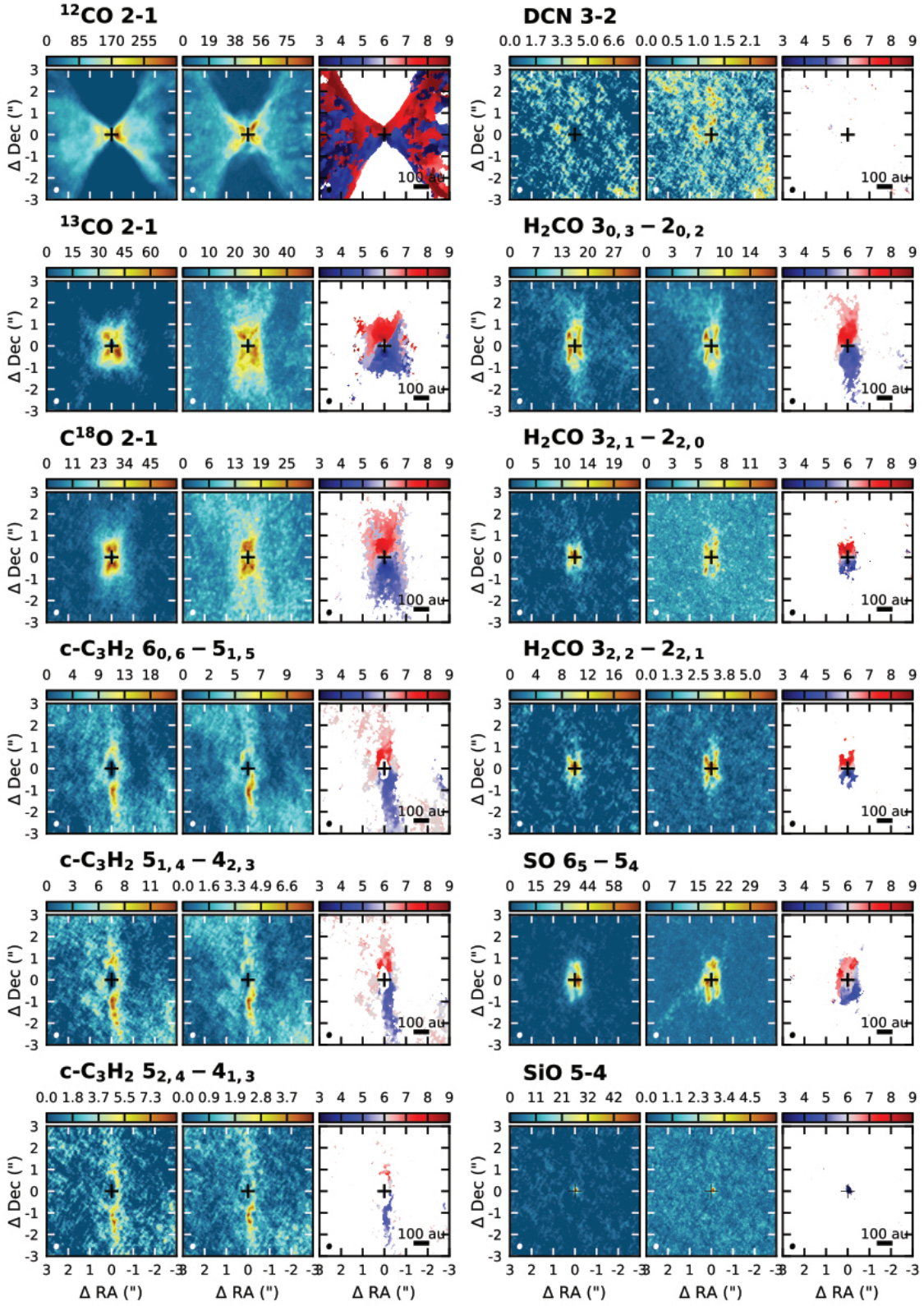


Figure 3. Overview of molecular lines detected toward L1527, shown on scales of the disk and inner envelope. The first and fourth column present integrated intensity (moment zero) maps (in $\text{mJy beam}^{-1} \text{ km s}^{-1}$), the second and fifth column present peak intensity (moment eight) maps (in mJy beam^{-1}), and the third and sixth column present velocity maps made with **bettermoments** (in km s^{-1} , centered at the systemic velocity of 5.9 km s^{-1}). The velocity map is only showing pixels above the $> 3\sigma$ level of the moment zero map. The molecular line is indicated above the panels, and the beam is depicted in the lower left corner of each panel.

served frequency of 225 GHz (Beckwith et al. 1990), and an average temperature of $T = 43 (L/L_{\odot})^{0.25}$ K = 46 K (with $L = 1.3 L_{\odot}$; Ohashi et al. subm.), based on a suite of radiative transfer models by Tobin et al. (2020). This results in a dust mass of $\sim 41 M_{\oplus}$. Adopting a temperature of 20 K, as typically done for Class II disks (e.g., Ansdell et al. 2016), results in a dust mass of $\sim 112 M_{\oplus}$. For a gas-to-dust ratio of 100, the total disk mass is then $\sim 0.01\text{--}0.03 M_{\odot}$, consistent with previous estimates at different wavelengths given different choices for temperature and dust opacity (e.g. Tobin et al. 2013; Aso et al. 2017; Nakatani et al. 2020; Sheehan et al. 2022). The here derived mass is a lower limit because the continuum emission is likely optically thick.

3.2. Molecular lines

An overview of all molecular lines detected towards L1527 is listed in Table 1 and presented in Fig. 3. In addition to moment zero maps (integrated intensity), we show moment eight maps (peak intensity) and velocity maps (similar to moment nine maps) created with the quadratic method of the `bettermoments` package² (Teague & Foreman-Mackey 2018). It is evident from Fig. 3 that each molecular species and for H_2CO , each transition, exhibits a different spatial and velocity distribution. Each species and its spatial origin (e.g., outflow, envelope, disk) is therefore discussed individually below (Sect. 3.2.1–3.2.6), before the full molecular structure and the underlying physical and/or chemical structure are discussed in Sects. 4.3 and 4.4.

3.2.1. ^{12}CO , ^{13}CO , C^{18}O

In addition to the images on disk-scales shown in Fig. 3, moment zero, moment eight and velocity maps on larger scales are presented in Fig. 4 for the CO isotopologues. The large-scale ^{12}CO emission displays an hour glass morphology, with emission originating along and inside the outflow cavity walls. The cavity walls deviate from a parabolic shape and display a kink (highlighted with white arrows in Fig. 4). This kink occurs at larger offsets from the source for the northwestern and southeastern cavity walls. The most prominent feature inside the cavity walls is visible $\sim 3\text{--}6''$ (420–840 au) west of the source position at blueshifted velocities (highlighted with an arrow in the velocity map in Fig. 4 and in the channel maps in Fig. B2).

^{12}CO emission is detected over a velocity range of $-11.3 - -1.13$ and $0.77 - 9.04$ km s^{-1} (with respect to the systemic velocity of 5.9 km s^{-1} Caselli et al. 2002; Tobin et al. 2011), while most of the emission is resolved

out at velocities close to the systemic velocity. There is no clear velocity gradient visible in the outflow direction (east–west), but the southern outflow cavity walls are more pronounced at blueshifted velocities, while the northern cavity walls are stronger at redshifted velocities. This velocity pattern is more clearly visible at smaller scales (Fig. 3) and is similar to the rotation direction of the disk and inner envelope.

The ^{13}CO and C^{18}O emission are dominated by the disk and inner envelope (Fig. 3), but they also have a contribution from material inside and along the cavity walls. Emission inside the cavity walls is clearly visible in the ^{13}CO images in Fig. 4 (at offsets larger than $\sim 4''$ in the east–west direction), while for C^{18}O it is only visible in the individual velocity channels (see Fig. B4). Large-scale emission is seen out to velocity offsets of $\sim |7.5|$ km s^{-1} in ^{12}CO emission, while this is only visible out to $\sim |2.0|$ km s^{-1} in ^{13}CO and C^{18}O , maybe due to the lower sensitivity at the higher velocity resolution. For both ^{13}CO and C^{18}O , there is a narrow arc of emission in both outflow cavities that moves outward with increasing velocity offsets (Figs. B3 and B4). A similar moving “front” of emission is also visible in a range of ^{12}CO channels (Fig. B2), but at smaller spatial scales ($\sim 2\text{--}3''$ off source, compared to $\sim 2\text{--}16''$ for ^{13}CO and C^{18}O) and higher velocity offsets ($\sim |2.5 - 7|$ km s^{-1} , compared to $\lesssim |2.0|$ km s^{-1} for ^{13}CO and C^{18}O). This differences between ^{12}CO and $^{13}\text{CO}/\text{C}^{18}\text{O}$ is likely because most ^{12}CO emission is resolved out at the velocities where the $^{13}\text{CO}/\text{C}^{18}\text{O}$ moving “front” is detected and the sensitivity is not high enough to detect $^{13}\text{CO}/\text{C}^{18}\text{O}$ emission at velocities as high as for ^{12}CO .

The large-scale C^{18}O moment eight map (Fig. 4) displays X-shaped emission ($\lesssim 8''$), while very faint and narrow X-shaped emission is visible in some ^{13}CO velocity channels (Fig. B1) and very weakly in the moment zero map on smaller spatial scales ($\lesssim 4''$). This structure was previously observed for $^{13}\text{CO } J = 1 - 0$ emission (Ohashi et al. 1997). One of the reasons for the difference between the ^{13}CO and C^{18}O moment maps is that while ^{13}CO (and ^{12}CO) emission is resolved out near the systemic velocity, C^{18}O is detected in all low-velocity channels. Therefore, to better compare the spatial origin of the emission from the different CO isotopologues, ^{13}CO and C^{18}O images are created at the same velocity resolution as the ^{12}CO image, and velocity channels with emission from all three isotopologues overlaid are presented in Fig. 5. Channel maps for each individual isotopologue are shown in Fig. B1. The overlay in Fig. 5 reveals a layered structure, with ^{12}CO tracing the surface layer of the cavity wall and ^{13}CO and C^{18}O tracing deeper and deeper into the envelope. The faint and narrow X-

² <https://github.com/richteaue/bettermoments>

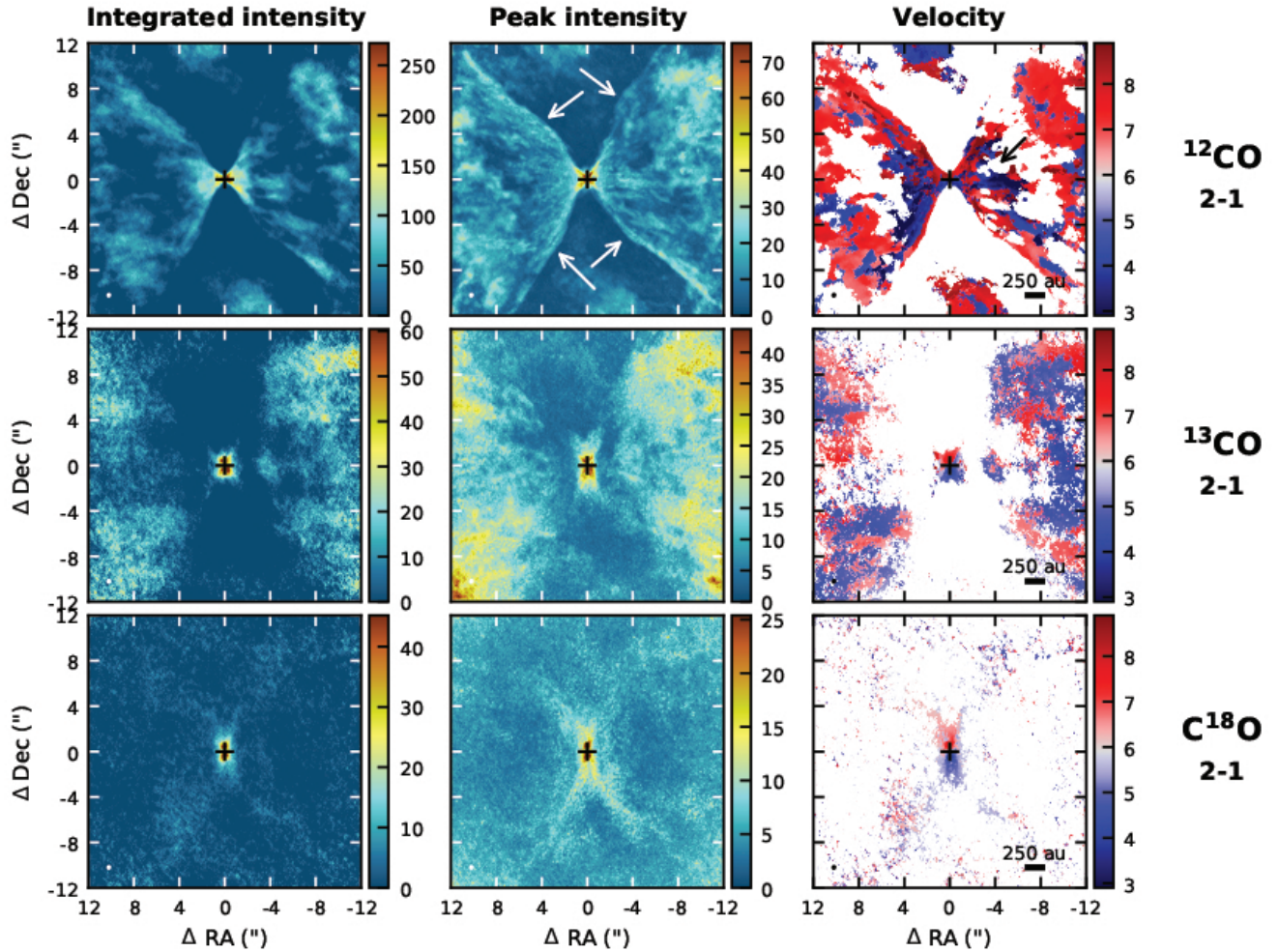


Figure 4. Overview of CO isotopologue emission at scales larger than depicted in Fig. 3. The first column presents integrated intensity (moment zero) maps (in $\text{mJy beam}^{-1} \text{ km s}^{-1}$), the middle column presents peak intensity (moment eight) maps (in mJy beam^{-1}), and the right column presents velocity maps made with `bettermoments` (in km s^{-1} , centered at the systemic velocity of 5.9 km s^{-1}). The color scale of the moment zero and moment eight maps are capped to highlight emission at large scales. The velocity map is only showing pixels above the $> 3\sigma$ level of the moment zero map. The beam is shown in the bottom left corner of each panel. The white arrows in the ^{12}CO peak intensity map (top middle panel) highlight the kinks discussed in the main text (Sect. 3.2.1), and the black arrow in the ^{12}CO velocity map marks the potential jet.

shaped emission visible in ^{13}CO channels coincides with ^{12}CO emission from the cavity wall (visible in yellow), while the broad X-shape in the C^{18}O moment maps is caused by emission at velocities close to the systemic velocity. A similar structure is visible for ^{13}CO at -0.5 km s^{-1} , and this velocity channel clearly shows that the ^{13}CO emission originates from layers closer to the outflow cavity. The emission from the inner envelope and disk, as traced by ^{13}CO and C^{18}O ($-1.77, -1.13, 0.77, 1.41 \text{ km s}^{-1}$ in Fig. 5), is present in between the ^{12}CO emission features. Here too, the ^{13}CO emission is peaking in higher layers compared to C^{18}O . The C^{18}O channel maps at the original velocity resolution (Fig. B4) clearly show that the emission has a contribution from outflowing material as well as from the surface layer of

the envelope or cavity wall. At velocities close to the systemic velocity ($\pm \sim 0.5 \text{ km s}^{-1}$), these components start to overlap.

While both ^{13}CO and C^{18}O trace emission from the disk and inner envelope, the contributions from the different components are not exactly the same for both isotopologues. The difference in origin between ^{13}CO and C^{18}O emission becomes more clear from position-velocity (pv) diagrams, as presented in Fig. 6. Emission at angular offsets $\gtrsim 2''$ as well as emission in the non-Keplerian quadrants (top left and bottom right) is relatively stronger for C^{18}O than for ^{13}CO . Together with the fact that ^{13}CO emission is resolved out in the central channel while C^{18}O emission is not, this suggests that C^{18}O traces emission from the infalling envelope

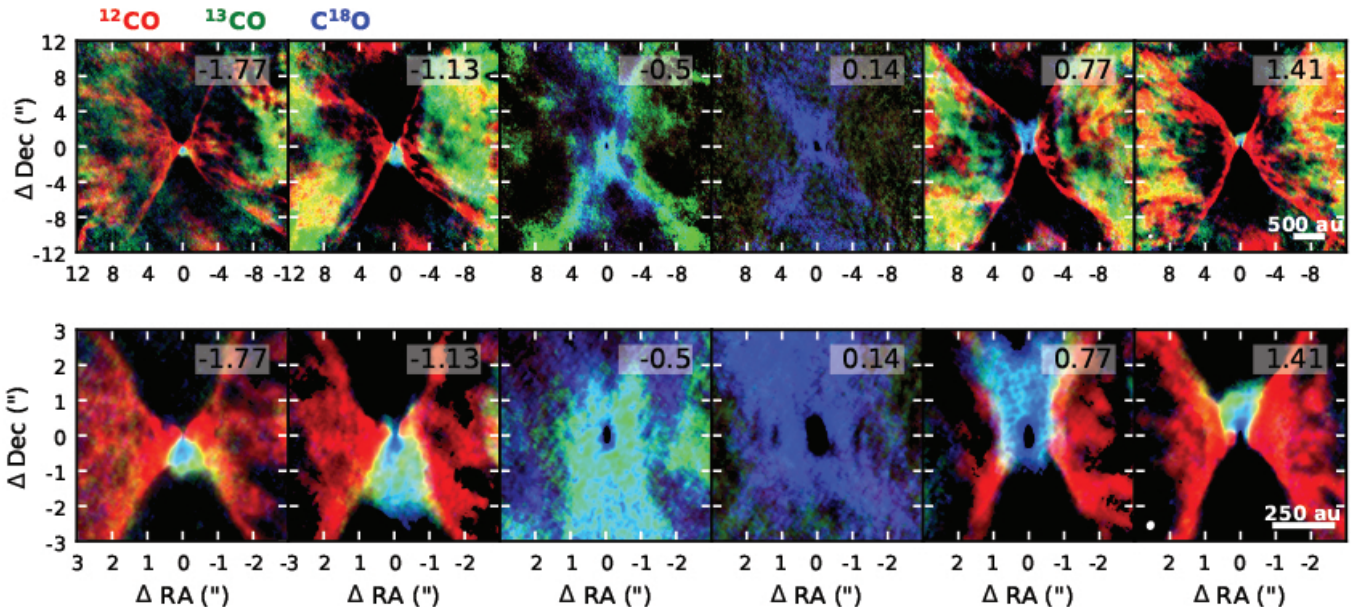


Figure 5. Selected velocity channel maps showing ^{12}CO (red), ^{13}CO (green) and C^{18}O (blue) emission overlaid. The bottom row is zoomed in on the central part of the channels shown in the top row. The velocity with respect to the systemic velocity is listed in the top right corner of each panel. The beam (nearly identical for all three isotopologues) is shown in the bottom left corner of the right most panels. The same channels are shown for each individual molecule in Fig. B1.

out to larger scales than ^{13}CO emission. This is probably because ^{13}CO becomes optically thick faster due to its higher abundance and hence gets resolved out more heavily near line center. Close to the central protostar, the C^{18}O emission is concentrated on scales $\lesssim 1''$ and velocities $\gtrsim 1 \text{ km s}^{-1}$, while ^{13}CO emission extends out to slightly larger scales and slightly lower velocities. This suggests that the contribution from the innermost envelope is stronger for ^{13}CO than it is for C^{18}O , likely due to the higher ^{13}CO abundance. A similar conclusion can be drawn from the velocity maps (Fig. 3), where ^{13}CO displays a stronger contribution from blueshifted envelope emission in the north and redshifted envelope emission in the south, that is, opposite to the disk velocity structure.

The intensity ratio between ^{13}CO and C^{18}O in channels with disk and inner envelope emission ($|\Delta v| \gtrsim 1 \text{ km s}^{-1}$) is $\sim 1\text{--}3$ instead of the canonical ratio of ~ 7 (Wilson & Rood 1994). This suggests that ^{13}CO is generally optically thick and that C^{18}O is probably optically thick in the midplane region where the line ratio is lowest (~ 1), consistent with earlier observations (van 't Hoff et al. 2018). The central negative “gap” visible in the ^{13}CO and C^{18}O moment zero map (and low-velocity channels, e.g., Fig. 5 and most clearly visible in Fig. B1) is therefore likely the result of continuum oversubtraction from optically thick line emission, potentially in combination with absorption by cold outer envelope material that is being resolved out.

3.2.2. SiO

Very compact, mostly unresolved SiO emission is detected just west of the source position, peaking at an offset of $-0''.08$ ($\sim 11 \text{ au}$; Fig 7). The emission is predominantly blueshifted and is detected at velocities ranging between -13.45 and 1.30 km s^{-1} with respect to the systemic velocity, and peaks at -2.72 km s^{-1} . This component is not seen in any of the other molecular lines. ^{12}CO emission typically peaks towards the northwest or southwest, rather than directly west, and emission close to source is only detected out to -10.18 km s^{-1} in individual velocity channels (see also Fig. 7, right panel). SiO is a shock tracer and is typically observed in protostellar jets. A jet origin of the SiO emission observed toward L1527 is consistent with the high velocities of the emission.

3.2.3. $c\text{-C}_3\text{H}_2$

All four $c\text{-C}_3\text{H}_2$ transitions (two are blended, see Table 1) display strong emission features along the north-south direction out to offsets of $\sim 2''$ (280 au ; Fig. 3), which is more extended than the bright components seen in ^{13}CO and C^{18}O ($\sim 1''$). The blueshifted emission in the south is stronger than the redshifted emission in the north. In contrast, the total extent in the east-west direction is only $\sim 0''.3$, compared to $\sim 1''.0$ and $\sim 2''.0$ for C^{18}O and ^{13}CO , respectively. In addition, a weak large scale emission component is visible (most clearly seen in Fig. 1).

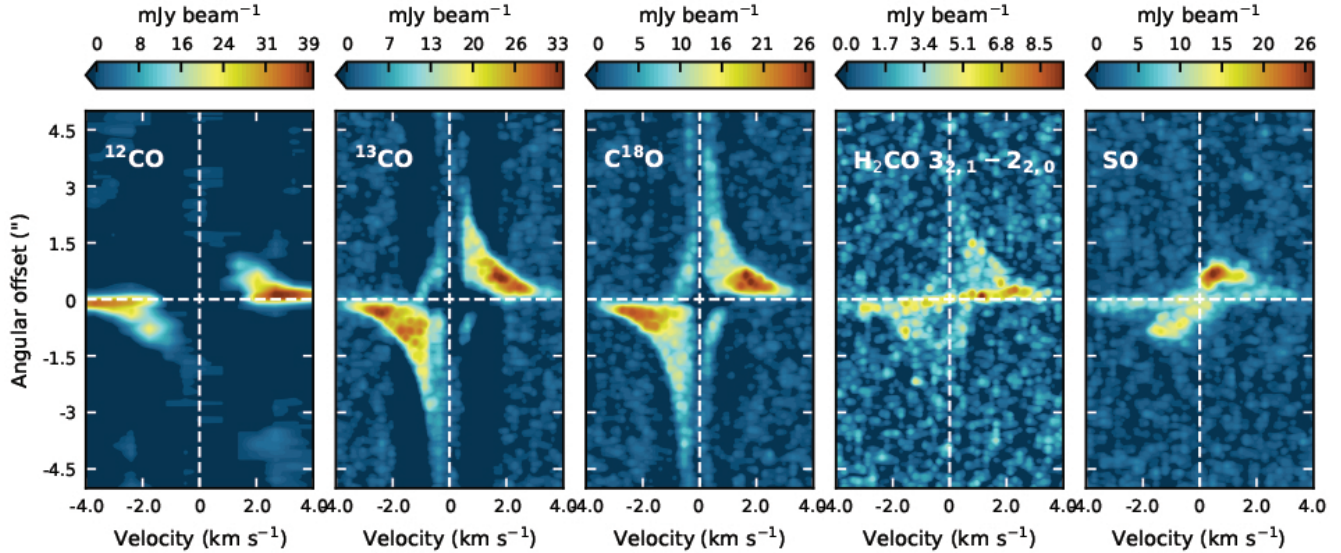


Figure 6. Position-velocity diagrams extracted along the major axis (averaged over the size of the beam) for ^{12}CO (first panel) and the molecular lines observed at 0.167 km s^{-1} resolution: ^{13}CO (second panel), C^{18}O (third panel), $\text{H}_2\text{CO } 3_{2,1} - 2_{2,0}$ (fourth panel), and SO (fifth panel). For ^{12}CO , a cropped velocity range is shown for better visibility of the structure of the other molecular lines. The horizontal and vertical dotted white lines mark the source position and systemic velocity (which is shifted to 0 km s^{-1}), respectively.

At the velocity resolution of 1.34 km s^{-1} , the $c\text{-C}_3\text{H}_2$ transitions are detected in only three channels, spanning a velocity range of $-1.16 - 1.53\text{ km s}^{-1}$, except for the blended $6_{0,6} - 5_{1,5}$ and $6_{1,6} - 5_{0,5}$ transitions that display weak ($3\text{--}4\sigma$) emission at -2.5 km s^{-1} (Fig. B5). The faint extended component is only visible in the central channel. The combination of emission morphology and narrow velocity range indicates that $c\text{-C}_3\text{H}_2$ is tracing envelope emission. A central absorption feature is only present in the central velocity channel and is likely due to absorption of the warm continuum emission by cold envelope material.

3.2.4. DCN

Very weak DCN emission is tentatively detected at the $3\text{--}4\sigma$ level in the central velocity channel (Fig. B6). The emission is extended surrounding a central region with negative emission and bears the most resemblance to the faint large scale emission component seen in $c\text{-C}_3\text{H}_2$ (as shown in Fig. 1). There is a hint of a narrow emission feature north of the source extending in the north–south direction in the first redshifted channel (1.53 km s^{-1}), but such a feature is absent in the south in the first blueshifted channel (-1.16 km s^{-1}). This is reflected in the peak intensity map shown in Fig. 3. DCN is thus at least present in the envelope and the central absorption feature is likely due to absorption of the warm continuum.

3.2.5. H_2CO

Three H_2CO transitions are observed, with upper level energies of 21 K ($3_{0,3} - 2_{0,2}$) and 68 K ($3_{2,1} - 2_{2,0}$ and $3_{2,2} - 2_{2,1}$). The low-energy transition displays stronger and more extended emission than the higher energy transitions. All transitions display X-shaped emission, extending about $0''.8$ toward the north and south, and $0''.4$ toward the east and west (Fig. 3; most clearly visible in the peak intensity maps). The low-energy transition ($3_{0,3} - 2_{0,2}$) shows an emission peak along the north–south axis at $\sim 1''$ offsets. This feature is smaller and less evident for the higher energy transitions. Only the $3_{0,3} - 2_{0,2}$ transition displays weak extended emission in the north–south direction as well as inside the outflow cavity walls ($\gtrsim 8''$).

The difference in emission morphology between the H_2CO transitions, as well as the origin of the emission can be more clearly seen in the individual velocity channels. In Fig. 8 we compare the $3_{0,3} - 2_{0,2}$ and $3_{2,2} - 2_{2,1}$ transitions because they are observed at the same low velocity resolution of 1.34 km s^{-1} . In order to provide a qualitative description of the origin of the H_2CO emission we also present velocity channel maps of a model with a Keplerian disk (125 au radius) embedded in a rotating and infalling envelope (CMU; Ulrich 1976; Cassen

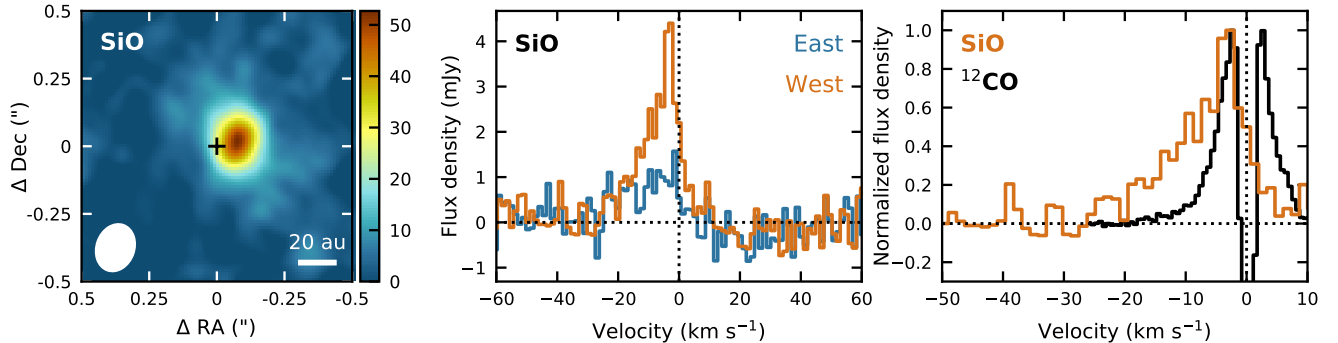


Figure 7. Integrated intensity (moment zero) map of SiO in the inner $0''.5$ (left panel) and spectra extracted in a $0''.2$ aperture (middle panel) centered on the SiO peak $0''.08$ west of the source position (orange) and at the same angular offset to the east (blue). In the right panel the normalized spectrum toward the SiO peak (orange) is compared to the normalized ^{12}CO spectrum extracted in the same aperture (black). The color scale of the integrated intensity map is in $\text{mJy beam}^{-1} \text{ km s}^{-1}$. The beam is depicted in the lower left corner and the cross marks the source position.

& Moosman 1981)³. The temperature and density structure are based on radiative transfer modeling of multi-wavelength continuum observations of L1527 by Tobin et al. (2013) and this model has been used by van 't Hoff et al. (2018, 2020, 2022) to study molecular line observations toward L1527. The model images are created with the radiative transfer code LIME (Brinch & Hogerheijde 2010). Our goal here is not to reproduce the observed emission exactly, but to illustrate the emission features expected for emission originating in different parts of the protostellar system. The model presented in Fig. 8 has emission originating in the inner 250 au of the envelope and in the surface layers of the disk.

The low-energy $3_{0,3} - 2_{0,2}$ transition is detected over a velocity range of $-3.84 - 2.87 \text{ km s}^{-1}$, while the high-energy transition is only marginally detected at -3.84 km s^{-1} (Fig. 8). The $3_{2,1} - 2_{2,0}$ transition is observed at a higher velocity resolution (0.167 km s^{-1}) and emission is detected over a velocity range of $-3.05 - 3.14 \text{ km s}^{-1}$ (Fig. B7), suggesting that the asymmetry in velocity for the other transitions is likely due to the low spectral resolution. The V-shaped emission pattern responsible for the X-shape in the integrated intensity map (Fig. 3) is visible in all channels, except the central channel, and is characteristic of emission originating in the surface layers of the disk. In contrast, the emission features $\sim 1''$ north and south of the source position

seen most strongly for $3_{0,3} - 2_{0,2}$ are only present in the -1.16 and 1.53 km s^{-1} channels and not at higher velocities, and likely originate in the inner envelope. Both transitions differ in the central velocity channel; where the $3_{2,2} - 2_{2,1}$ emission extends to the east and west in a bow-tie pattern, the $3_{0,3} - 2_{0,2}$ transition shows absorption surrounded by compact emission features to the southeast and northwest. The bow-tie pattern of $3_{2,2} - 2_{2,1}$ is indicative of disk emission, while the asymmetric features, as well as the more extended features at low velocities in the north and south of $3_{0,3} - 2_{0,2}$, are consistent with envelope emission. The $3_{2,2} - 2_{2,1}$ bow-tie extends as far in the east and west direction as the $3_{0,3} - 2_{0,2}$ emission features, so the absence of the bow-tie for the $3_{0,3} - 2_{0,2}$ transition is not due to the central absorption. The warm $3_{2,2} - 2_{2,1}$ transition thus originates predominantly in the disk surface layers, while the colder $3_{0,3} - 2_{0,2}$ transition also has a strong contribution from the envelope. Absorption of continuum emission by the outer envelope is then the likely origin of the absorption in the central velocity channel of the $3_{0,3} - 2_{0,2}$ transition.

3.2.6. SO

Emission from the SO $6_5 - 5_4$ transition ($E_{\text{up}} = 35 \text{ K}$) is detected over a velocity range of $-4.05 - 3.30 \text{ km s}^{-1}$ (Fig. B8), and extends about $1''$ north and south of the source position in the integrated and peak intensity maps (Fig. 3). At low velocities ($-0.54 - 0.46 \text{ km s}^{-1}$), weak more extended emission is visible (see Figs. 9 and B9). These narrow arc-like emission features extend predominantly towards the southwest and are blueshifted, but less extended ($\lesssim 4''$) X-shaped emission is visible. This large scale emission overlaps with

³ The CMU model describes the collapse of an isothermal, spherically symmetric, and uniformly rotating cloud. The assumption of free fall with each particle conserving angular momentum results in particles moving along parabolic paths. Details about the implementation can be found in Appendix C of van 't Hoff et al. (2018).

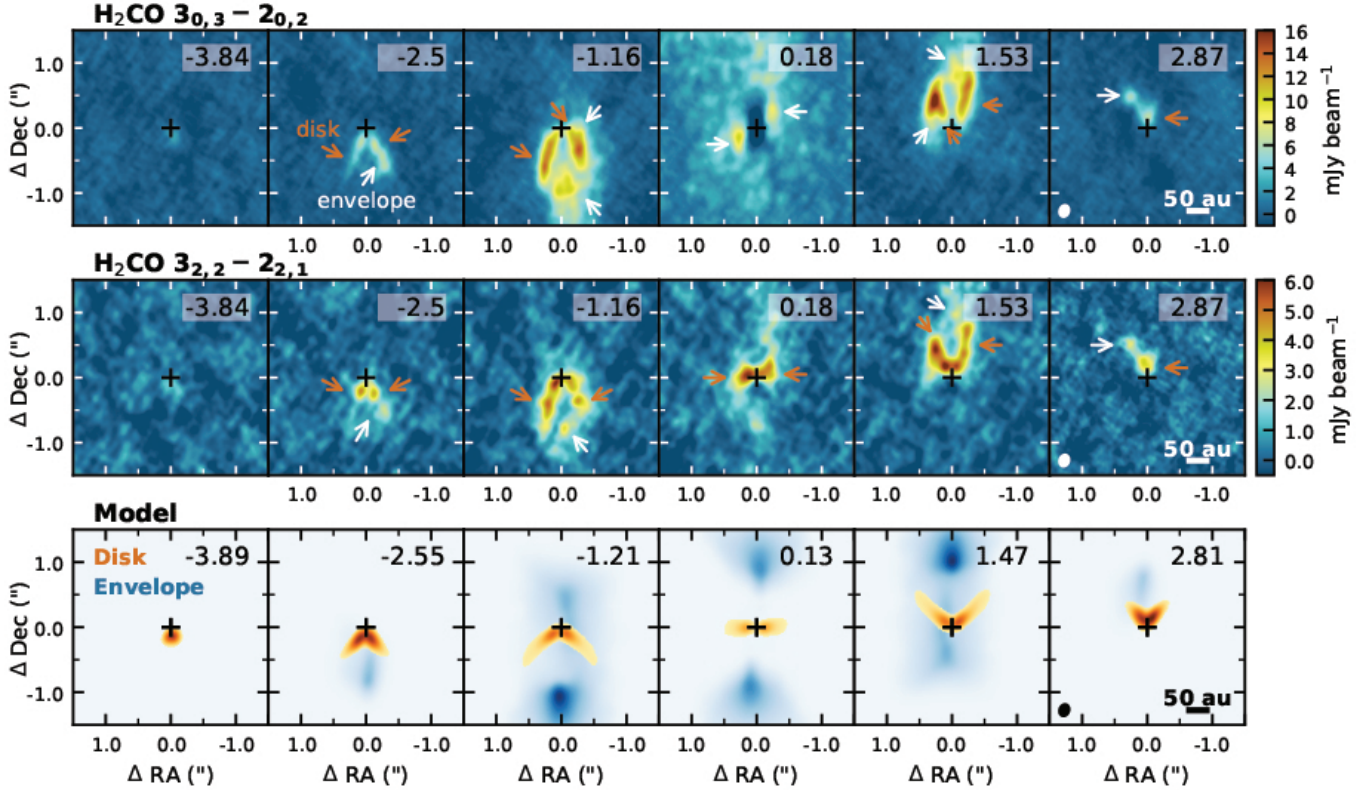


Figure 8. Velocity channel maps for the H_2CO $3_{0,3} - 2_{0,2}$ (top row) and $3_{2,2} - 2_{2,1}$ (middle row) transitions, and for a model of a 125 au (radius) Keplerian rotating disk embedded in a rotating infalling envelope with molecular line emission originating in the disk surface layers and the inner envelope (bottom row; Tobin et al. 2013; van ’t Hoff et al. 2018, 2020, 2022). In the model panels, the contribution from the disk is shown in an orange color gradient and the envelope contribution is shown in a blue color gradient. For visualization purposes, the disk emission is depicted on top of the envelope emission. The model is meant as a qualitative comparison to determine the origin of the H_2CO emission. Observed emission features most likely originating in the disk surface are marked by orange arrows, and envelope features by white arrows. The black cross marks the source position. The velocity with respect to the systemic velocity is listed in the top right corner of each panel. The beam is shown in the bottom left corner of the right most panels.

the surface layer of the envelope traced in C^{18}O . However, the SO emission originates in a more narrow layer in individual velocity channels. Due to the rotating, infalling velocity profile of the envelope, emission from the surface layer has a slightly different spatial location at different velocities, resulting in the double layered feature in the southwest in the peak intensity map (Fig. 9, arrow in top right panel). The narrow SO emission feature visible in the southeastern outflow cavity in the peak intensity map (Fig. 9, arrow in bottom right panel) is not visible in the C^{18}O map, but it is formed by small SO emission patches over a velocity range of $-0.54 - 0.13$ km s^{-1} that coincide with the outward moving emission front visible in ^{13}CO and C^{18}O channels (Figs. B4 and B3). Several more of such SO emission spots coinciding with the outflowing material traced in ^{13}CO and C^{18}O are visible at higher velocities and larger spatial offsets, especially in the western outflow cavity (Fig. B9).

The SO emission on $1''$ scales does not resemble the morphology of any of the other lines (Fig. 3). The north-south emission features east and west of the source position are more parallel to each other than the X-shape seen in H_2CO and do not extend as far east-west as ^{13}CO and C^{18}O . In addition, the SO emission peaks directly east and west of the source in the integrated intensity map (with the west side being brighter), while ^{13}CO and C^{18}O clearly peak north and south of source with less emission originating directly to the east and west. From the p - v -diagram (Fig. 6) it becomes clear that the redshifted emission is brighter than the blueshifted emission. Based on the channel maps (Fig. 10), this is most likely because there is redshifted emission present along the midplane at an offset of $\sim 1''$, while this is not the case at blueshifted velocities (e.g. 0.46 km s^{-1} versus -0.54 km s^{-1}).

The velocity structure as shown in Fig. 3 deviates from pure Keplerian rotation with blueshifted veloci-

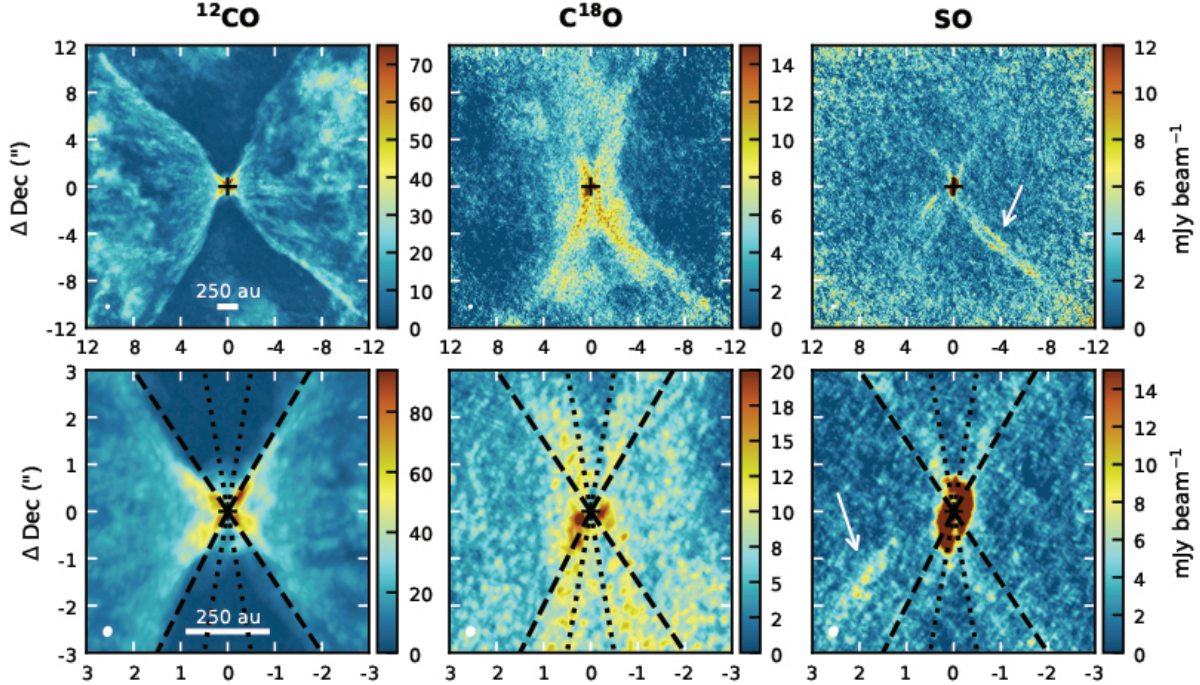


Figure 9. Moment eight (peak intensity) maps for ^{12}CO (left panels), C^{18}O (middle panels) and SO (right panels) on a scale of $24''$ (top panels) and $6''$ (bottom panels). For C^{18}O and SO , only the five central velocity channels ($-0.37 - 0.29 \text{ km s}^{-1}$) are used to highlight the large-scale emission features, while for ^{12}CO the full velocity range ($-11.3 - 9.04 \text{ km s}^{-1}$) has been used. The dashed and dotted lines are the same in all three bottom panels and are meant to help guide the eye with respect to the location of the emission. The white arrows point to features described in the main text. The beam is shown in the bottom left corner of each panel.

ties extending north of the source in the west and redshifted velocities extending south in the east. A similar pattern is seen for ^{13}CO , C^{18}O , $c\text{-C}_3\text{H}_2$, and $\text{H}_2\text{CO } 3_{0,3} - 2_{0,2}$ and indicates the presence of envelope emission. The pv-diagrams (Fig. 6) show that this envelope component is less extended than for ^{13}CO and C^{18}O as the SO emission is confined to smaller angular offsets. The SO pv-diagram consists of two components, most clearly distinct at blueshifted velocities, that seem to anti-correlate with the C^{18}O emission. The first component is a narrow feature at low spatial offsets ($\lesssim 0''.4$) that extends over the entire detected velocity range. A similar, but stronger, feature is also visible for H_2CO that originates predominantly in the disk surface layers, suggesting that this feature traces emission from the disk surface. The second feature is located at lower velocities ($\lesssim 2 \text{ km s}^{-1}$) and larger spatial offsets and is just offset from the region with bright C^{18}O emission, suggesting that it originates in the inner envelope or outer disk.

To look at the spatial origin of the SO emission in more detail we present selected velocity channel maps in Fig. 10 (the full velocity range is presented in Fig. B8) and overlay the 3σ contour of the SO emission on C^{18}O and $\text{H}_2\text{CO } (3_{2,1} - 2_{2,0})$ channels. At high redshifted velocities ($1.13 - 2.47 \text{ km s}^{-1}$), the SO emission displays

a V-shape resembling the H_2CO emission and coinciding with the outermost layer of C^{18}O emission. A similar pattern is visible at blueshifted velocities ($-2.38 - -1.88 \text{ km s}^{-1}$), although the emission is more asymmetric and dominated by the west side of the disk. This morphology is consistent with the conclusion drawn from the pv-diagrams that part of the SO emission originates in the disk surface layers.

At lower velocities the emission is predominantly located in two narrow bands extending north–south both east and west of source. Similar features are present in C^{18}O channels on top of more extended emission. Only at low redshifted velocities ($0.29 - 0.69 \text{ km s}^{-1}$) SO emission is visible along the midplane between $\sim 0''.5 - 1''.0$ north of source, coinciding with the low energy $\text{H}_2\text{CO } (3_{0,3} - 2_{0,2})$ transition. A model with emission originating solely in the surface layers of both the disk and envelope can explain the vertical emission bands at intermediate velocity offsets (e.g., -1.54 and 1.46 km s^{-1}), but not at velocities close to the systemic velocity (Fig. 10). This could be because there is a disconnect at the disk–envelope interface between the velocity structure in a model with a pure Keplerian disk and CMU envelope. Figure 10 also shows results for a model with emission arising solely from the disk–envelope interface. In this

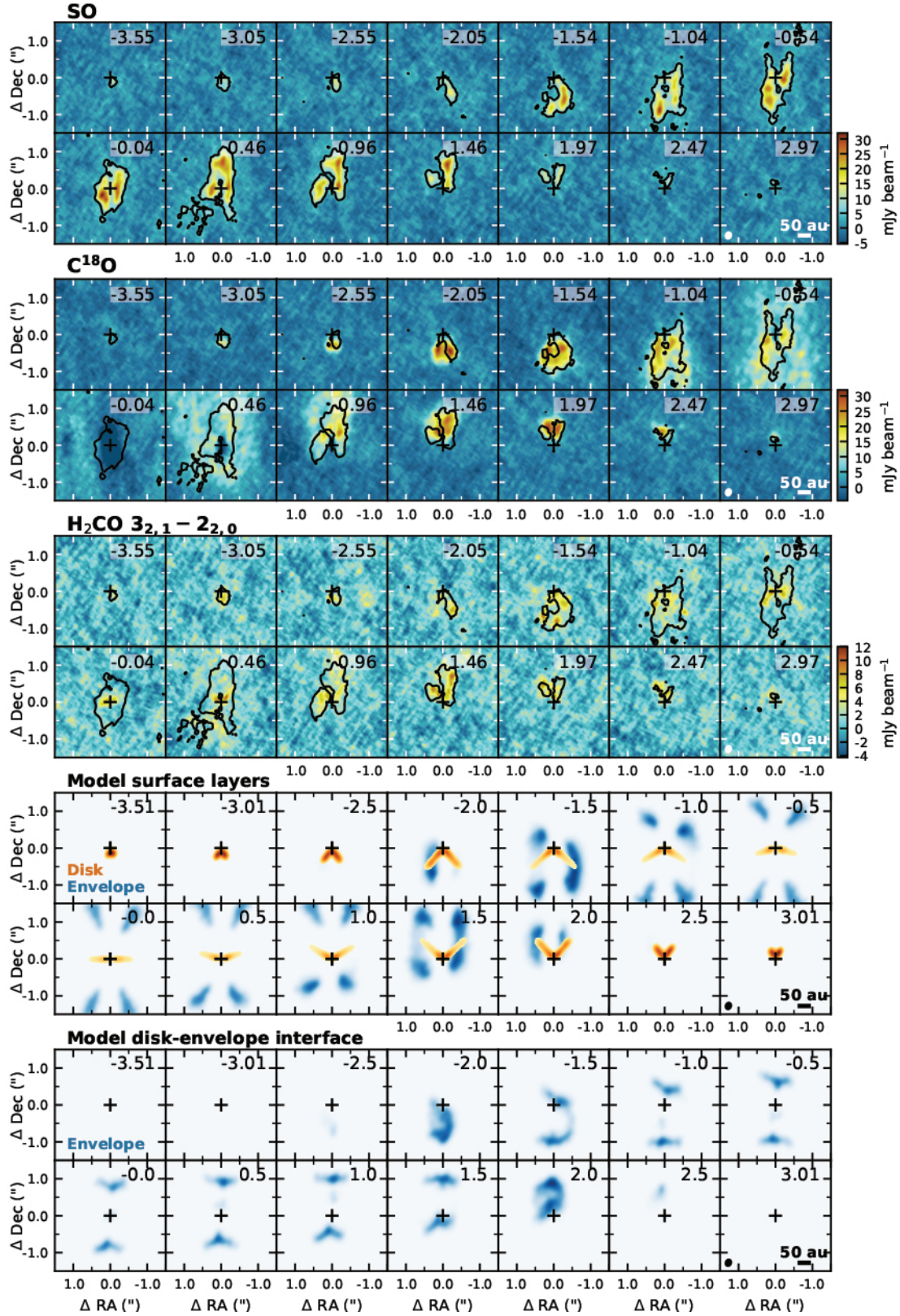


Figure 10. Selected velocity channel maps of the 0.167 km s^{-1} resolution data cubes for SO (top group of panels), C^{18}O (second group of panels), and $\text{H}_2\text{CO } 3_{2,1} - 2_{2,0}$ (third group of panels). The black contour marks the 3σ level of the SO emission in all panels. The fourth and fifth group of panels show velocity channel maps for a model with emission arising in the surface layers of both the disk (orange) and envelope (i.e., along the cavity wall; blue), and for a model with emission arising at the disk-envelope interface, i.e., in the inner envelope (125–150 au), respectively. The black cross marks the source position. The velocity with respect to the systemic velocity is listed in the top right corner of each panel. The beam is shown in the bottom left corner of the right most panels.

scenario, the majority of the emission is expected along the major axis of the system, which does not resemble the observed emission morphology. Overall, the SO emission thus seems to originate in the disk and inner envelope, and in both components the emission seems to originate predominantly in the surface layers.

4. ANALYSIS AND DISCUSSION

4.1. Continuum sub-structures and inclination

The L1527 disk displays smooth, but asymmetric continuum emission, with the southern side brighter than the northern side along the major axis, and the eastern side brighter than the western side. The image does not show the clumps previously reported in 7 mm VLA images (Nakatani et al. 2020), consistent with more recent higher signal-to-noise VLA images at the same wavelength and spatial resolution (Sheehan et al. 2022).

The north–south asymmetry was previously observed at 7 mm and 1.3 cm with the VLA, and confirmed through analytic modeling (Sheehan et al. 2022). As discussed by those authors, determining the underlying physical nature of this asymmetry is difficult due to the edge-on nature of the disk, and could depend on where the emission at different wavelengths becomes optically thick. Detailed modeling of multi-wavelength data is therefore required to assess whether there is an enhancement in surface density in the southern part of the disk and if so, whether this is related to for example a vortex, spiral or pressure bump. The east–west asymmetry was not visible in the VLA data, even though they have comparable spatial resolution, potentially because at these longer wavelengths the vertical extent of the disk is smaller and the emission is less optically thick.

Both asymmetries were recently observed with ALMA in Band 7 (0.87 mm) and Band 3 (3.3 mm), although with the western side brighter in Band 3 (Ohashi et al. 2022b). The same Band 3 data was presented by Nakatani et al. (2020), but they show that the brightness temperature peaks slightly southeast of the source position. We therefore re-imaged the archival Band 3 data with the eDisk data reduction and imaging scripts, which results in an image with the eastern side brighter than the western side (Fig. A2), similar to the Band 6 and 7 images. For a near-edge on disk like L1527, the disk can either be orientated such that eastern side faces us, in which case the emission east of source traces the back side of the disk, that is, the half of the disk furthest away from us along our line of sight, or such that the western side faces us, in which case the emission west of source traces the back or far side of the disk (see e.g., Fig. 6 in Oya et al. 2015). An asymmetry along the minor axis of a near-edge on disk can be explained by

a vertically extended optically thick dust disk. In this scenario, warmer material is observed toward the back side of the disk because the emission would get optically thick already in the colder outer disk on the near side (e.g., Ohashi et al. 2022b and Fig. 3 therein, Lin et al. *subm.*, Takakuwa et al. *in prep.*). The north–south asymmetry appears stronger at 3.3 mm, especially in the east, while the east–west asymmetry is less pronounced at longer wavelengths and only visible in the south. A stronger east–west asymmetry at shorter wavelengths hints that it is indeed due to optically thick emission, as the disk becomes less optically thick at longer wavelengths. However, the resolution of the Band 3 data is slightly lower than the here presented Band 6 data ($0''.086 \times 0''.043$ versus $0''.056 \times 0''.029$) and detailed modeling of the continuum emission at multiple wavelengths in the visibility plane is required to confirm the origin of east–west asymmetry. Nonetheless, the images presented here suggest that the continuum presents a coherent picture at different ALMA wavelengths, implying that the eastern side is the back side of the disk under the assumption of optically thick emission.

The brightness asymmetry of the disk previously observed in the Gemini L' (3.8 μm) scattered light image, with the eastern side nearly twice as bright as the western side, also suggests that the eastern side is the side facing us (Tobin et al. 2010). Deconvolution of the Spitzer IRAC image (3.6 μm) results in the western side being brighter (Velusamy et al. 2014), but the brightness of the cavities in scattered light has been shown to be variable over time (Tobin et al. 2008; Cook et al. 2019). The recently released JWST NIRC*am* image (release id 2022-055, proposal id 2739, PI: K. Pontoppidan⁴) also suggests that the eastern side is facing us. The JWST 4.4 μm image (Fig. 11) is consistent with the Gemini image⁵ and there is more short wavelength emission (2 μm) in the eastern cavity, which indicates less extinction and hence that the eastern cavity is the blue-shifted outflow cavity.

The orientation inferred from the dust continuum and scattered light is at odds with the orientation derived from molecular line emission from the envelope (CS;

⁴ <https://webbtelescope.org/contents/news-releases/2022/news-2022-055>

⁵ The ALMA continuum seems slightly rotated with respect to the JWST 4.4 μm image and is not located in the center of the dark lane between the two bright regions east and west of the source position in the 4.4 μm image. The JWST image aligns with the Spitzer IRAC image presented by Tobin et al. (2008) and there is no rotation evident based on the location of background stars. The east–west misalignment is not due to proper motion as L1527 is moving south, but the displacement is too small to rule out a systematic offset in the NIRC*am* image using the Spitzer image.

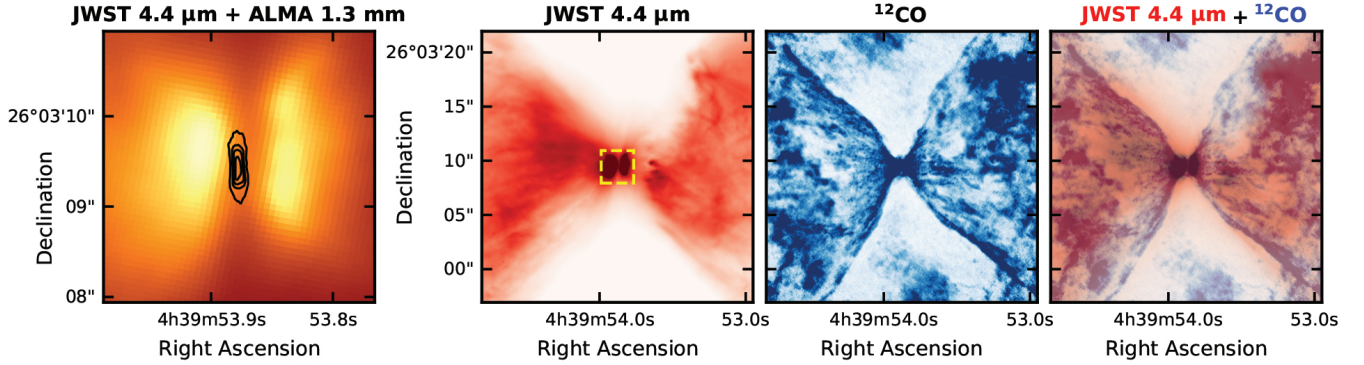


Figure 11. Comparison between the ALMA 1.3 mm continuum and ^{12}CO images and the JWST NIRCcam 4.4 μm image. The 4.4 μm image is shown on different spatial scales in the first and second panel, with the 1.3 mm continuum overlaid in contours in the first panel. The dashed yellow square in the second panel marks the region shown in the first panel. The ^{12}CO peak intensity (moment 8) map is shown in the third panel, and an overlay of the 4.4 μm image (red) and the ^{12}CO map (blue) is shown in the fourth panel.

Oya et al. 2015), which suggests that the western side is the back side. In this orientation, the blueshifted envelope emission is stronger in the southwest than in the southeast, while redshifted emission is stronger in the northeast than in the northwest. For a system with the eastern side being the back side, the blueshifted and redshifted envelope components would be strongest in the southeast and northwest, respectively. The velocity patterns of ^{13}CO , C^{18}O , $c\text{-C}_3\text{H}_2$, $\text{H}_2\text{CO } 3_{0,3} - 2_{0,2}$ and SO observed here (Fig. 3) are consistent with the earlier CS observations and suggest that the western side of the envelope is the far side.

However, a small inclination toward the west, as suggested by the continuum observations, is consistent with the large scale ($\sim 100''$) outflow observed in ^{12}CO , which shows blueshifted emission predominantly toward the east and redshifted emission toward the west (Hogerheijde et al. 1998). Consistent with previous observations, on smaller scales as observed here, the ^{12}CO emission displays both blueshifted and redshifted emission on both sides of the source, making it hard to infer the systems inclination. The potential blueshifted jet feature in the west (Fig. 4), as well as the blueshifted SiO emission in the west (Fig. 7), would suggest an orientation opposite of that based on the large scale outflow. However, in the ^{12}CO velocity channels, weak features are visible at high redshifted velocities in the extension of the potential jet.

Overall, the continuum emission on small scales ($\lesssim 0''.5$), the scattered light images, and the large-scale ^{12}CO outflow ($\sim 100''$) suggest that the eastern side of the system is facing us, while molecular line emission on small scales (SiO jet) and intermediate scales (envelope) are consistent with the opposite orientation of the western side facing us. Differences in orientation based on

outflowing material on small and large scales could be due to precession of the outflow, as discussed in more detail by Oya et al. (2015). The continuum asymmetry is observed at scales of $\sim 0''.1$, while the orientation derived from the line emission is based on envelope scales. This suggests that there is either a misalignment between the disk and the envelope, or a warp in the inner disk (Cook et al. 2019; Sakai et al. 2019). A detailed analysis of the molecular line emission on disk-scales may be able to help constrain the system's orientation. Moreover, an overlay of the ^{12}CO outflow cavity on the JWST NIRCcam 4.4 μm image shows that the asymmetry in the scattered light cavity shapes is not reflected in the ^{12}CO cavity walls, and may thus be the result of shadowing on the northwestern and southeastern cavity wall (Fig. 11). A comprehensive study including the molecular line emission, the multi-wavelength continuum emission, and the scattered light images is therefore required to fully unravel the structure of the system.

4.2. Dynamical mass and disk radius

The stellar mass and disk radius can be derived by fitting a double power law to the rotation curve (e.g., Seifried et al. 2016; Aso & Machida 2020; Maret et al. 2020). We use the publicly available Spectral Line Analysis/Modeling (SLAM) code⁶ to extract the rotation curves from the ^{13}CO and C^{18}O pv-diagrams (Aso et al. 2015; Sai et al. 2020) and to do the fitting. The signal-to-noise ratio of the H_2CO and SO emission is not high enough for this analysis and ^{12}CO is dominated by outflow emission. Details of the methods employed by SLAM are described by Ohashi et al. (subm.), but the main steps are as follows.

⁶ <https://github.com/jinshisai/SLAM>

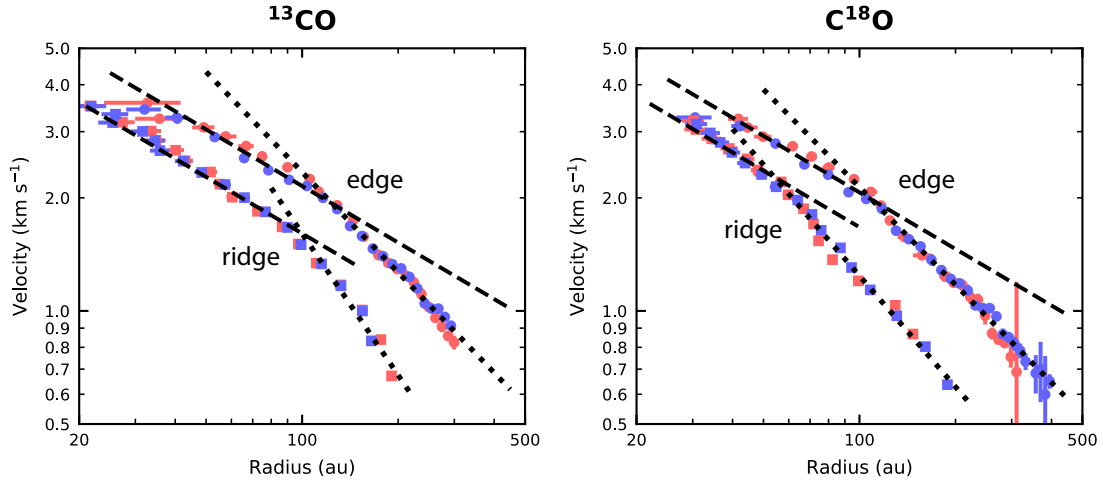


Figure 12. Rotation curves derived from the pv-diagrams along the disk major axis (Fig. 6) for ^{13}CO (left panel) and C^{18}O (right panel). Points tracing the outer edge of the pv-diagrams are shown as circles and points tracing the peak of the emission (the ridge) are shown as squares. Blue and red symbols denote blueshifted and redshifted emission, respectively. The dashed lines show power laws with indices, p_{in} , of -0.5 (for Keplerian rotation), and the dotted lines show power laws with the best-fit indices, p_{out} , as listed in Table 2. The radius where the two power laws cross, r_b , is listed in Table 2. The velocity is with respect to the systemic velocity.

Table 2. Results from the pv-diagram analysis.

Method	v_{sys}^a (km s^{-1})	Double power law			Inner power law fixed ($p_{\text{in}} = 0.5$)		
		p_{in}^b	p_{out}^c	r_b^d (au)	p_{out}^c	r_b^d (au)	M_*^e (M_{\odot})
^{13}CO edge	5.955 ± 0.005	0.43 ± 0.02	0.89 ± 0.03	114 ± 4	0.89 ± 0.02	125 ± 3	0.53 ± 0.02
^{13}CO ridge	6.024 ± 0.006	0.63 ± 0.01	1.57 ± 0.08	131 ± 3	1.25 ± 0.03	100 ± 2	0.29 ± 0.01
C^{18}O edge	5.958 ± 0.006	0.47 ± 0.03	0.86 ± 0.04	102 ± 6	0.86 ± 0.02	109 ± 5	0.49 ± 0.03
C^{18}O ridge	5.995 ± 0.007	—	—	—	0.98 ± 0.02	54 ± 2	0.32 ± 0.02

Notes. ^a Systemic velocity. ^b Power-law index of the inner power law. ^c Power-law index of the outer power law. ^d Transition radius between the inner and out power law. ^e Central mass.

First, the (position,velocity) coordinates are determined either for points tracing the outer edge (5σ level) of the pv-diagram or for points tracing the peak of the emission (also called the “ridge” of the pv-diagram). Next, a double power law is fit to the (position,velocity) coordinates using the Markov Chain Monte Carlo (MCMC) algorithm implemented in the `emcee` package (Foreman-Mackey et al. 2013). For an infalling rotating envelope conserving angular momentum, the velocity is proportional to r^{-1} , while for a Keplerian disk, $v \propto r^{-0.5}$. In the latter case the stellar mass can be derived from $v_b = \sqrt{GM_*/r_b} \sin i$, where v_b is the velocity at the transition radius, r_b , between disk and envelope velocity profiles. We first perform the fits with the systemic velocity and inner power-law index as free parameters and confirm that the power-law index for the inner region is indeed ~ -0.5 . We then fix

the systemic velocity to the best-fit value and the inner power-law index to -0.5 to derive the dynamical stellar mass. The results are listed in Table 2 and the rotation curves are shown in Fig. 12.

The dynamical mass derived from the two isotopologues is consistent within $1-2\sigma$, and is $\sim 0.3 M_{\odot}$ using the ridge method and $\sim 0.5 M_{\odot}$ using the edge method. This is higher than the $0.2 M_{\odot}$ derived by Tobin et al. (2012) from ^{13}CO and consistent with $0.45 M_{\odot}$ derived by Aso et al. (2017) from C^{18}O , who used the ridge method on lower resolution data. For the edge points, the transition radius found from ^{13}CO and C^{18}O is also consistent with each other within error bars, while the results from the ridge points are different for the two isotopologues and different from the edge point derived values. The reason is most likely that the ridge is not well defined at this high resolution (see the pv-diagrams in

Fig. 6). The difference between ^{13}CO and C^{18}O for the ridge points could also be due to the difference in optical depth between the two isotopologues resulting in both isotopologues tracing a different layer. An average radius of 108 au from the edge points is only slightly larger than the radius derived from the C^{18}O pv-diagram by Aso et al. (2017) (75 au). Tobin et al. (2012) derived a 125 au disk radius from multi-wavelength continuum modeling, but the 5σ contour of the 1.3 mm image extends only out to ~ 85 au. A detailed analysis of the continuum emission is required to better constrain the dust-disk size, but it seems not very different from the gas-disk size. Overall, the analysis for L1527 seems most robust using the edge method and suggests a stellar mass of $\sim 0.5 M_{\odot}$ and a gas-disk radius of ~ 110 au.

4.3. Temperature structure

4.3.1. The disk is too warm for CO freeze out

On scales of a few arcseconds, both ^{13}CO and C^{18}O display an X-shaped emission morphology (most clearly visible in the peak intensity maps in Fig. 4), with emission arising from the surface of the envelope along the outflow cavity wall out to larger radii than emission from the midplane. Along the midplane, the emission starts to disappear at offsets of $\sim 2''.5$ (~ 350 au), suggesting that CO starts to freeze out. This is consistent with the analysis of ^{13}CO , C^{18}O and C^{17}O by van 't Hoff et al. (2018, 2020), which showed that CO was present in the gas phase throughout the entire disk (~ 100 au), as well as with the temperature profile derived from modeling the multi-wavelength continuum emission by Tobin et al. (2013) in which the temperature drops below 20 K at a radius of 360 au.

A more detailed temperature structure can be obtained from the optically thick ^{13}CO brightness temperature as presented in Fig. 13. For all channels with velocities $\gtrsim |1| \text{ km s}^{-1}$ and with resolved emission, the brightness temperature is higher than 20 K, with temperatures increasing in the surface layers up to ~ 50 K. The temperature in the radially and vertically most extended regions is < 20 K, but this is likely due to the emission becoming optically thin (especially in the upper most surface layers) and beam dilution as this region typically fills only half of the beam. Beam dilution is also the reason why temperatures decrease at velocities $\gtrsim |3| \text{ km s}^{-1}$, where the emission solely originates in the inner half of the disk. Based on the $^{13}\text{CO}/\text{C}^{18}\text{O}$ line ratio, the C^{18}O emission is only optically thick in the midplane at angular offsets $\lesssim 0''.5$. Consequently, the midplane brightness temperatures are consistent with those for ^{13}CO , while the brightness temperature in the surface layers is lower ($\sim 30\text{--}35$ K). These results are also

in agreement with the disk midplane temperature profile derived by van 't Hoff et al. (2018) from observations with lower resolution and sensitivity.

The temperature structure can also be assessed using H_2CO . The resolution is high enough to spatially resolve a decrease in H_2CO toward the midplane, as observed before for the edge-on young disk IRAS 04302 (Podio et al. 2020; van 't Hoff et al. 2020). Assuming this is due to freeze out, the base of the V-shape provides an estimate of the H_2CO snowline at ~ 70 K (Noble et al. 2012; Fedoseev et al. 2015). The tip of the V is unresolved, suggesting that the snowline is at a radius less than 24 au. In addition, the ratios of H_2CO lines are good probes of temperature (e.g., Mangum & Wootten 1993). Fig. 14 (top row) presents the $3_{0,3} - 2_{0,2}/3_{2,2} - 2_{2,1}$ line ratio per channel, and shows that the ratio is $\lesssim 3$ in all pixels with a $> 3\sigma$ detection of the weaker $3_{2,2} - 2_{2,1}$ transition.

The $3_{0,3} - 2_{0,2}/3_{2,2} - 2_{2,1}$ ratio as observed here is particularly sensitive to temperatures $\lesssim 90$ K (see Fig. C1). For optically thin emission in Local Thermodynamic Equilibrium (LTE), the ratio drops from ~ 20 to ~ 5 for temperatures between 20 and 40 K. Around 90 K the ratio has dropped to ~ 3 , and the ratio remains higher than 2 for temperatures up to 300 K. If the emission is optically thick, the ratio drops below 2. The observed line ratio is > 2 , except in the inner $\sim 0''.3$, where the emission thus becomes optically thick. A conservative estimate of the uncertainty on the line ratio in the optically thin regions (ratio > 2) with a $> 6\sigma$ detection of the $3_{2,2} - 2_{2,1}$ transition is then 18% when propagating the individual rms noise levels of the observations. This means that for line ratios of ~ 3 , the temperature is at least 60 K, but the upper limit is not well constrained. As can be seen from Fig. 14, the temperature in the regions where both H_2CO lines are detected is then at least 60 K. At velocity offsets of -1.16 and 1.53 km s^{-1} , no $3_{2,2} - 2_{2,1}$ emission is detected from the midplane and the ratio becomes $\gtrsim 4$, suggesting temperatures below ~ 40 K. In the inner envelope midplane where both transitions are detected (angular offsets of $\sim 0''.75\text{--}1''.0$) temperatures of at least 60 K are found. A similar temperature was derived in this region from a non-LTE large-velocity-gradient (LVG) analysis of SO by Ohashi et al. (2014); Sakai et al. (2014b).

The temperatures derived from the H_2CO line ratio are $\sim 10\text{--}20$ K higher than the ^{13}CO brightness temperature. This difference is likely caused by two dominant effects. First, the brightness temperature from ^{13}CO traces the radius where the emission gets optically thick. This is not necessarily the same as the observed angular offset, which means that colder material further out may be projected closer to the star. Second, the bright-

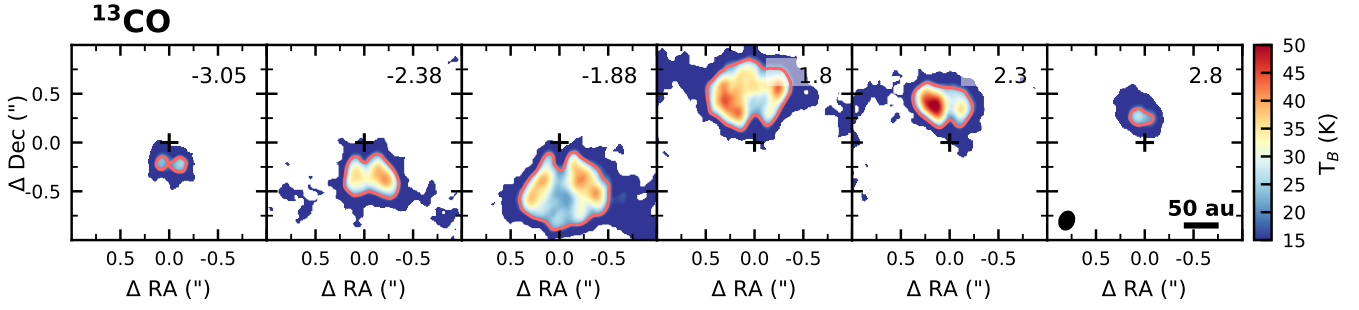


Figure 13. Brightness temperature of ^{13}CO in selected 0.167 km s^{-1} velocity channels. Only pixels above the 3σ level are shown. The red line marks the 20 K contour. The velocity with respect to the systemic velocity is listed in the top right corner of each panel. The beam is shown in the bottom left corner of the right most panel.

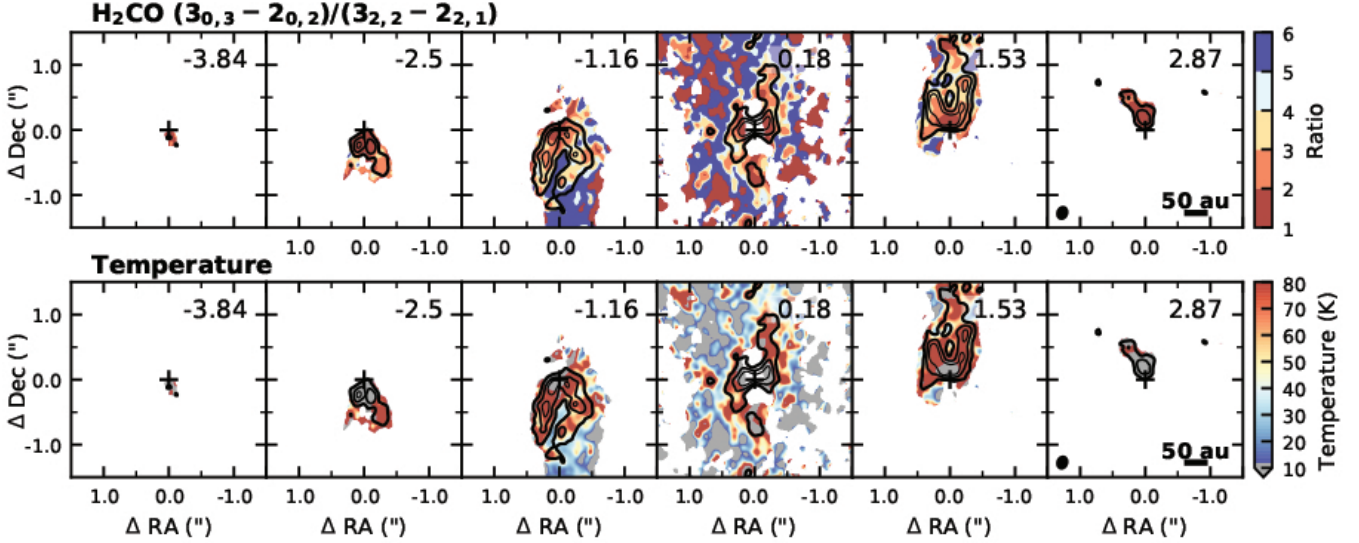


Figure 14. Line ratio of the $\text{H}_2\text{CO } 3_{0,3} - 2_{0,2}$ and $3_{2,2} - 2_{2,1}$ transitions in the observed velocity range (top panels) and the corresponding temperature for optically thin emission (bottom panels). Ratios lower than 2 indicate optically thick emission and those regions are shown in grey in the temperature maps (bottom panels). Only pixels with a $> 3\sigma$ detection of the $3_{0,3} - 2_{0,2}$ transition are shown, and the contours depict the 3, 6 and 9σ levels of the $3_{2,2} - 2_{2,1}$ transition. The color scale is such that blue indicates low temperatures (corresponding to high ratios) and red indicates high temperatures (corresponding to low ratios). The black cross marks the source position. The velocity with respect to the systemic velocity is listed in the top right corner of each panel. The beam is shown in the bottom left corner of the right most panels.

ness temperature of the ^{13}CO emission gets smeared out over the size of the beam, while the effects of beam dilution cancel out for the H_2CO line ratio. Since both effects work to lower the observed brightness temperature of ^{13}CO , the physical temperature is likely closer to that measured with H_2CO . In addition, while the brightness temperature of the continuum drops steeply at radii $\gtrsim 0''.3$, continuum subtraction may have lowered the ^{13}CO brightness temperature a little. A higher mid-plane temperature than derived from the ^{13}CO brightness temperature would be consistent with the analysis by [van 't Hoff et al. \(2018\)](#) that showed that the temperature profile as derived by [Tobin et al. \(2013\)](#) from the multi-wavelength continuum emission needed to be increased by at least 30% to reproduce the observations.

Such a warm temperature profile was also adopted by [Aso et al. \(2017\)](#) for analysis of C^{18}O observations of L1527.

Finally, if the dust is optically thick, as suggested by the brightness asymmetry along the minor axis, the continuum brightness temperature provides a third temperature probe. The continuum brightness temperature is $\sim 40 \text{ K}$ out to $\sim 25 \text{ au}$, after which it steeply drops to temperatures below $\sim 20 \text{ K}$ (Fig. 2), probably because the emission becomes optically thin. A midplane temperature of $\sim 40 \text{ K}$ at 25 au is consistent with the ^{13}CO brightness temperatures at larger radii and the temperature profile derived by [van 't Hoff et al. \(2018\)](#). However, the continuum brightness temperature suffers from the same effects as the ^{13}CO brightness temperature, so it

may also underestimate the real temperature. Overall, all results point to the L1527 disk being warm, with midplane temperatures too high for CO freeze out throughout the disk (20–40 K), but low enough for H₂CO freeze out outside ~ 24 au.

Moreover, the similarity between the temperature derived from the continuum and the molecular lines suggests that the grains do not scatter efficiently, as this would decrease the brightness temperature (Birnstiel et al. 2018). Since grains only scatter appreciably when the size of the grain is comparable to the observing wavelength, this suggests that L1527 mainly contains grains much smaller than ~ 1 mm. The lack of large grains is consistent with the vertical extent of the dust disk which indicates that the grains have not yet settled.

4.3.2. A potential temperature enhancement around the disk–envelope interface

At intermediate redshifted velocities (e.g., the 1.8 km s^{−1} channel shown in Fig. 13), the ¹³CO brightness temperature increases from ~ 25 K to ~ 35 K at angular offsets $\gtrsim 0''.5$ ($1\sigma = 2$ K). A similar effect is derived from the H₂CO line ratio, but at both redshifted and blueshifted velocities. This suggests that there may be an increase in temperature around the disk–envelope interface. Such a rise was invoked by Sakai et al. (2014b) based on SO observations. Temperatures of ~ 60 K and ~ 200 K were derived from SO emission at angular offsets between $\sim 0''.6$ – $1''.0$ (Ohashi et al. 2014; Sakai et al. 2014b, 2017, resp.), but these studies did not have high enough spatial resolution and signal-to-noise ratio to derive a temperature at smaller offsets. However, there is no increase in ¹³CO brightness temperature at blueshifted velocities, so several factors have to be taken into account before a temperature enhancement can be concluded from the observations presented here.

Relating the brightness temperature observed at a certain position in a certain velocity channel to a physical location is non-trivial, because it depends on where in the system the emission becomes optically thick (see e.g., Fig. 6 in van ’t Hoff et al. 2018). For example, if the emission along a line of sight close to the protostar becomes optically thick in the outer envelope, the brightness temperature at a small angular offset will reflect the temperature in the cold outer envelope instead of in the warm disk. Since redshifted emission originates in the rotating-infalling envelope in front of the disk, and blueshifted emission in the envelope behind the disk, a comparison between redshifted and blueshifted velocity channels can help constrain the origin of the emission. If the emission becomes optically thick in the disk, the redshifted and blueshifted channels should be similar. However, this is inconsistent with the observations. The

two simplest possible scenarios are then that either the ¹³CO emission is just optically thick ($\tau \gtrsim 1$), or that the ¹³CO is very optically thick ($\tau \gg 1$).

The first scenario ($\tau \gtrsim 1$) could explain the observations if the ¹³CO emission becomes optically thick in the envelope behind the disk at blueshifted velocities, and in the disk at redshifted emission. In other words, if the disk itself does not contain enough CO to make the emission optically thick. The observations would then suggest that the envelope midplane (seen at blueshifted velocities) is colder than the outer disk midplane (seen at redshifted velocities). A potential issue with this scenario is that it may not be able to reproduce the (marginally) optically thick C¹⁸O emission.

The second scenario ($\tau \gg 1$) may explain the observations if the ¹³CO emission already becomes optically thick in the envelope at redshifted velocities and in the disk at blueshifted velocities. In this case there is enough material in both the envelope and the disk to make the emission optically thick. This would then suggest that the disk midplane (seen at blueshifted velocities) is colder than the inner envelope (seen at redshifted velocities). If the C¹⁸O emission does not become optically thick yet in the envelope (at redshifted velocities), this temperature increase would not be visible in C¹⁸O, consistent with the observations. A potential inconsistency is that you would expect to observe warm emission from the inner envelope at angular offsets larger than the extent of the disk at both blueshifted and redshifted velocities. The fact that this is not observed, suggests then that either the temperature or the optical depth drops quickly in the inner envelope. However, a rapid decrease in temperature is inconsistent with the temperature derived from H₂CO, which shows ~ 60 K out to $\sim 1''.1$ – $1''.4$ (~ 150 – 200 au projected from the source), and a rapid decrease in optical depth is inconsistent with the observed ¹³CO/C¹⁸O line ratio, which suggests ¹³CO is optically thick out to $\sim 1''.1$ – $1''.4$ as well.

An alternative explanation for the ¹³CO observations is that there is a north–south asymmetry in the temperature, but this would be opposite to the north–south asymmetry observed for the continuum emission and not clearly visible in H₂CO. In conclusion, both the ¹³CO and H₂CO show potential evidence of an increase in the temperature in the outer disk and/or inner envelope. However, observations of H₂CO at higher spectral resolution and for higher energy transitions are required to better constrain the temperature. Moreover, detailed radiative transfer modeling is required to derive a temperature structure for the disk and envelope from the observed emission and to confirm whether an increase in temperature occurs at the disk–envelope interface.

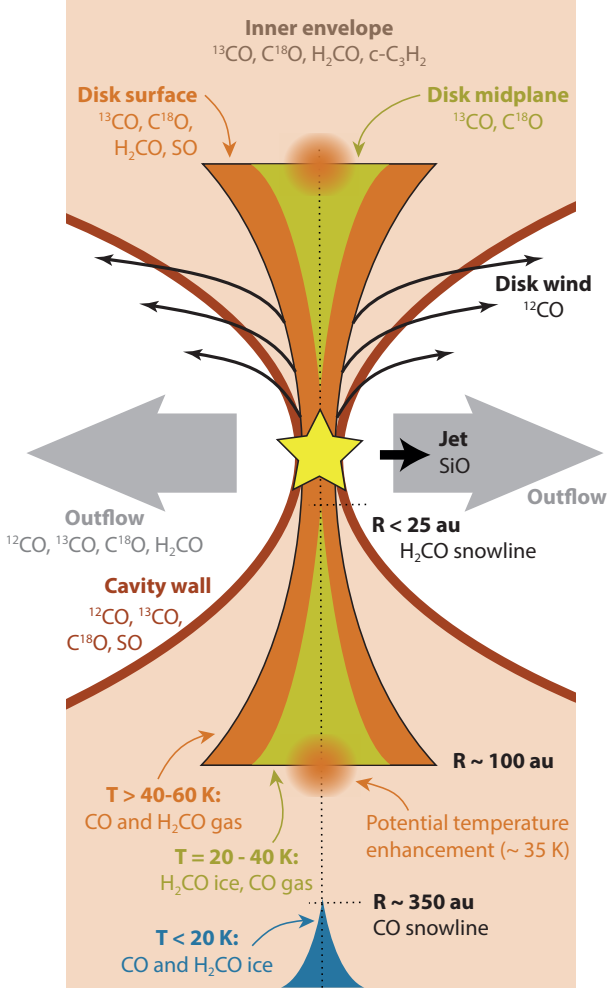


Figure 15. Schematic overview of the chemical and temperature structure of the inner few hundred au of the L1527 protostellar system based on the observations presented here. The potential temperature enhancement is seen in both the north and south in H_2CO , but only in the north in ^{13}CO .

4.4. Molecular structure

A cartoon illustrating which components of the L1527 protostellar system are traced by which molecules is presented in Fig. 15. Outflowing material is visible in ^{12}CO , ^{13}CO , C^{18}O , and H_2CO $3_{0,3} - 2_{0,2}$ with ^{12}CO tracing the highest velocity gas. A blueshifted jet is visible in the western outflow cavity in SiO and potentially ^{12}CO . The SiO jet is compact and located close to the protostar (peak position is $0''.08$ offset from source), while the ^{12}CO jet is further away from the source ($\sim 3-6''$) and extended in the east–west direction. The outflow cavity wall is clearly outlined in ^{12}CO , but also faintly in ^{13}CO (at small scales), C^{18}O and SO. The large scale envelope is visible in $\text{c-C}_3\text{H}_2$ and weakly in DCN. Emission from the inner envelope is most strongly visible in ^{13}CO . In

addition, while weak envelope emission is seen in H_2CO $3_{0,3} - 2_{0,2}$, all H_2CO transitions display bright emission in the inner envelope midplane. The disk is traced by ^{13}CO , C^{18}O and H_2CO , where H_2CO only originates in the disk surface layers. SO also traces surface layers in the disk and inner envelope, that is, in layers along the outflow cavity wall. The physical and/or chemical reason behind the different emission morphologies is further discussed in the following sections.

4.4.1. Outflowing material

All three CO isotopologues display a moving front of emission in the outflow cavity with material at higher velocities located further away from the star (marked with dotted lines in the channel maps in Figs. B2-B4). This is in agreement with both a jet/bow shock driven outflow as well as a wind-driven outflow (e.g., Lee et al. 2000; Arce et al. 2007, and references therein). The velocity maps in Fig. 3 show that the ^{12}CO emission has higher velocities along the outflow cavity walls close to source ($\lesssim 1''$) compared to the disk emission traced by ^{13}CO and C^{18}O , suggesting that there may be a disk wind in this system. The velocity structure can be shown more clearly in pv-diagrams obtained parallel to the disk minor axis at different offsets along the major axis, that is, north and south of the source position (Fig. 16). ^{13}CO and C^{18}O show Keplerian emission on one side of the diagram and a low-velocity contribution from the envelope in the other half. In contrast, ^{12}CO shows extended emission in all four quadrants but peaks near the ^{13}CO and C^{18}O disk emission. However, the bright ^{12}CO emission has velocities higher than the expected Keplerian velocity. The fainter extended ^{12}CO emission may be explained by material moving away in a conical or parabolic shape. Because the outflow is in the plane of the sky, the near side of this shell would move toward us and the far side would move away from us, resulting in both redshifted and blueshifted emission. This poloidal expansion coupled with the super-Keplerian rotation suggests that ^{12}CO may trace a rotating, expanding disk wind. A more detailed analysis is left for future work.

The outward moving front is present in both outflow cavities for ^{13}CO and C^{18}O , while ^{12}CO only shows this in the eastern cavity (Figs. B2-B4, but outside of the angular range shown in the pv-diagrams in Fig. 16). Instead, there is an indication of a blueshifted ^{12}CO jet $\sim 3-6''$ ($\sim 400-800$ au) off source (Figs. 4 and B2). However, the velocity is lower than the velocity of the SiO jet closer to source (~ 11 au). ^{12}CO emission has been observed before with CARMA ($\sim 3''$ resolution) and ALMA ($0''.8$ resolution) in the $J = 1 - 0$ transi-

tion (Flores-Rivera et al. 2021), which displays a similar outflow morphology as the $J = 2-1$ transition presented here. Flores-Rivera et al. (2021) referred to the narrow ‘neck’ between the two outflow cavities (see Figs. 3, 11, B2, fourth row) as a jet extending out to ~ 75 au. However, the channel maps in Fig. B2 (fourth row) suggest a widening of the outflow opening angle with the north-south extension (making up the ‘neck’) originating from emission copatial with the disk and/or inner envelope (potentially tracing a wind) with redshifted emission north of the source and blueshifted emission south of the source. At larger scales (Fig. B2), there is a hint of a redshifted jet-like emission feature along the line of the blueshifted jet at larger offsets ($\sim 8-12''$). This may signal that the jet has precessed. Precession may also explain the kinks seen in the outflow cavity walls (marked by white arrows in Fig. 4). Alternatively, this could be due to widening of the outflow opening angle over time, or due to inhomogeneity of the surrounding medium.

4.4.2. Disk versus envelope

Studying whether changes occur in the composition of the volatile material as it transitions from the envelope to the disk is crucial for understanding the origin of chemical complexity in planet-forming material. Moreover, identifying molecular species or transitions that exclusively trace the disk environment would aid in identifying and studying the conditions in young disks. In recent years, chemical changes across the disk–envelope interface have been observed for multiple sources (e.g., L1527, L1489, IRAS 16293 A, IRAS 16293 B, IRAS 15398; Sakai et al. 2014b; Yen et al. 2014; Oya et al. 2016, 2018; Okoda et al. 2018, resp.), but so far no molecule or transition has been uniformly identified that reliably traces the disk or the disk–envelope interface.

In the observations presented here, $c\text{-C}_3\text{H}_2$ emission originates solely in the envelope. The $c\text{-C}_3\text{H}_2$ observations are consistent with previous ALMA observations of different transitions (Sakai et al. 2014b) and the distribution of C_2H (Sakai et al. 2014a). These hydrocarbons are often associated with UV irradiation and therefore typically observed in photo-dissociation regions (PDRs; e.g., van der Wiel et al. 2009; Guzmán et al. 2015) and along outflow cavity walls, especially in Class 0 sources (e.g., Murillo et al. 2018; Tychoniec et al. 2021). At the spectral resolution of 1.34 km s^{-1} , strong $c\text{-C}_3\text{H}_2$ emission is only detected in three 1.34 km s^{-1} velocity channels ($-1.16 - 1.53 \text{ km s}^{-1}$), but weak (3σ) emission is detected at -2.5 km s^{-1} for the blended $6_{0,6} - 5_{1,5}$ and $6_{1,6} - 5_{0,5}$ transitions, which is at a higher velocity offset than detected before (-2.2 km s^{-1} ; Sakai et al.

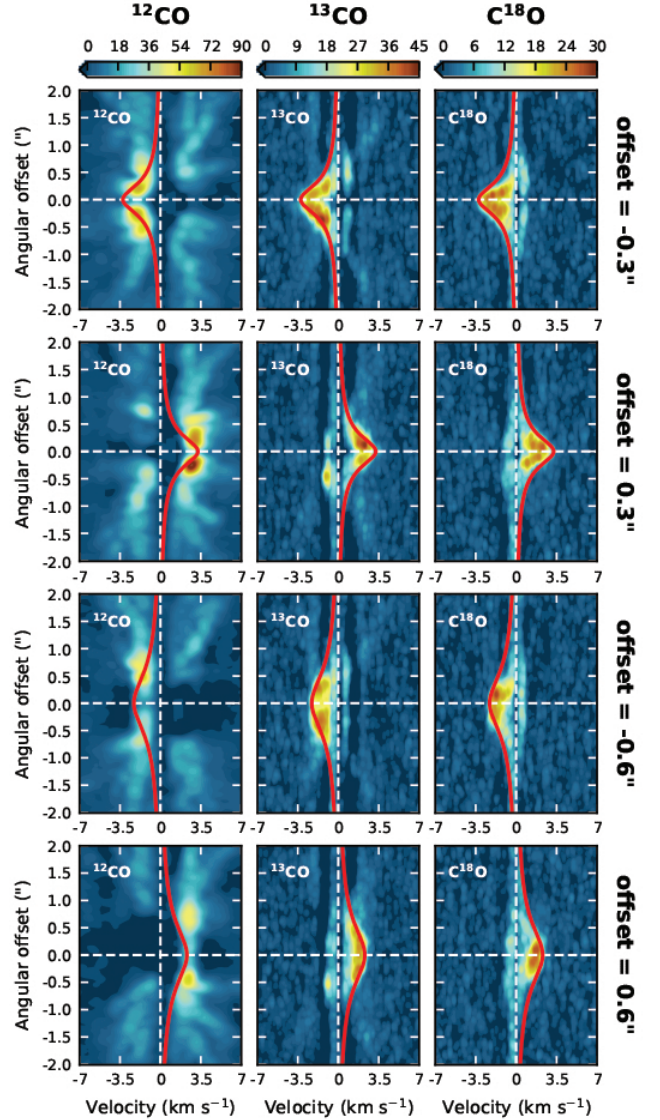


Figure 16. Position-velocity diagrams of the CO isotopologues (different columns) extracted parallel to the disk minor axis (averaged over the size of the beam) at offsets of $\pm 0''.3$ (first and second row) and $\pm 0''.6$ (third and fourth row) along the major axis (i.e., north and south of the source position). The horizontal dotted line marks the disk midplane, with larger angular offsets corresponding to the disk surface layers. The vertical dotted line marks the systemic velocity, which is shifted to 0 km s^{-1} . The red curve shows the expected Keplerian velocity for a $0.5 M_{\odot}$ star (based on the pv-diagram analysis described in Sect. 4.2) at each radial offset, r , as function of disk height, z : $V_{\text{Keplerian}} = \sqrt{\frac{GMr^2}{(r^2+z^2)^{3/2}}}$ (e.g. Rosenfeld et al. 2013).

2014b). Higher spectral resolution observations are required to constrain the distribution in the envelope, and higher sensitivity observations are needed to establish whether $c\text{-C}_3\text{H}_2$ is really absent in the disk. The pres-

ence or absence of $c\text{-C}_3\text{H}_2$ in the disk is interesting as bright hydrocarbon emission in Class II protoplanetary disks is associated with high C/O ratios (> 1 ; [Bergin et al. 2016](#); [Miotello et al. 2019](#)). A comparison between embedded and mature disks could thus provide information about the chemical evolution during the disk stage.

The H_2CO transitions observed here predominantly originate in the disk surface layers, where the temperature as determined from the line ratio is $\gtrsim 60$ K. The higher energy transitions ($3_{2,1} - 2_{2,0}$ and $3_{2,2} - 2_{2,1}$) are not detected in the midplane, while weak emission from the lower energy transition ($3_{0,3} - 2_{0,2}$) is present. The $3_{0,3} - 2_{0,2}$ flux is expected to increase at lower temperatures (for a given column density), so this is not an excitation effect. The observed distribution could instead be due to freeze out of H_2CO in the midplane as the freeze-out temperature is ~ 70 K ([Noble et al. 2012](#); [Fedoseev et al. 2015](#)). A low residual midplane abundance could be due to gas-phase formation of H_2CO or nonthermal desorption (e.g., [Aikawa et al. 2002](#); [Loomis et al. 2015](#); [Öberg et al. 2017](#); [Terwisscha van Scheltinga et al. 2021](#)). Alternatively, the $3_{0,3} - 2_{0,2}$ emission along the midplane originates in the envelope that is visible between the disk surface layers. These results substantiate the analysis of the temperature profile of the young disk IRAS 04302 based on a similar V-shaped emission pattern of one H_2CO transition toward that source ([van 't Hoff et al. 2020](#)). The increase in H_2CO intensity in the inner envelope (or outer disk, as detailed modeling is required to determine the exact location) could then be due to a lower freeze-out temperature at lower densities or an increase in temperature at the disk-envelope interface (as discussed in Sect. 4.3.2).

SO has been suggested to be enhanced at the centrifugal barrier in L1527, due to elevated temperatures in this region caused by an accretion shock (e.g., [Sakai et al. 2014b, 2017](#)). While the concept of a centrifugal barrier is not supported by hydrodynamic simulations, the physics and dynamics at the disk-envelope interface are complex ([Jones et al. 2022](#); [Shariff et al. 2022](#)), and models show that SO can be enhanced if a shock occurs ([Aota et al. 2015](#); [Miura et al. 2017](#); [van Gelder et al. 2021](#)). Consistent with previous observations, SO emission is strong at scales $\lesssim 1''$, and in the region of the pv-diagram consistent with the outer disk and/or inner envelope. However, a careful examination of the individual velocity channels suggests that the emission is coming from surface layers of the envelope (i.e., along the cavity wall) rather than the midplane. This is, for example, clearly visible at -1.54 km s^{-1} , where H_2CO $3_{2,1} - 2_{2,0}$ displays emission from the disk surface layers and the envelope midplane, while the SO emission sur-

rounds the H_2CO envelope midplane emission (Fig. 10, but see also Fig. 8). The SO emission pattern is also inconsistent with a simple model with emission from the inner envelope (Fig. 10, fifth set of panels), and shows better agreement with a model where the emission solely originates in the surface layers of the disk and envelope (Fig. 10, fourth set of panels).

Based on the H_2CO line ratio, the temperature in the disk surface layers is $\gtrsim 60$ K, so the origin of the SO emission could be thermal sublimation of SO ice as the freeze out temperature of SO is $\sim 40\text{--}60$ K ([Hasegawa & Herbst 1993](#); [Garrod & Herbst 2006](#)). Thermal sublimation may also explain why there is some SO emission present along the midplane at $\sim 0''.7$ at low redshifted velocities ($0.46\text{--}0.96 \text{ km s}^{-1}$), as the ^{13}CO brightness temperature is increased in this region. However, the increase in ^{13}CO brightness temperature is visible at higher velocities ($\sim 1.8 \text{ km s}^{-1}$; Fig. 13), while there is no SO emission along the midplane at those velocities. Alternatively, SO may trace UV irradiated environments, either because of UV heating of the gas causing SO ice to desorb, or because its formation becomes possible in these regions through photodissociation of H_2O . It is possible to form SO in shocks, which may occur at the disk-envelope interface and/or along the outflow cavity wall, but this still requires the presence of a UV field ([van Gelder et al. 2021](#)). If the distribution of SO is set by the UV field, this may naturally lead to an enhancement in the inner envelope as UV radiation may penetrate deeper into the envelope than into the disk. However, a detailed study is required as the disk could shadow parts of the inner envelope. An SO distribution along the outflow cavity wall was also inferred for the embedded disk TMC1A ([Harsono et al. 2021](#)). Observations of multiple SO transitions are needed to derive the temperature of the emitting gas and detailed modeling will be required to fully constrain the spatial and physical/chemical origin of the SO emission.

5. CONCLUSIONS

We have presented high resolution ($0''.06\text{--}0''.17$ or $8\text{--}24$ au) ALMA observations (taken as part of the Large Program eDisk) of the 1.3 mm continuum and molecular line emission toward the Class 0 protostar L1527, and provided a qualitative description of the different emission morphologies and their potential underlying physical and/or chemical conditions. The main conclusions are summarized below:

- The continuum emission is smooth, but asymmetric along both the major (north-south) and minor axis (east-west), with emission being brighter in the south and east. The flaring nature of the disk

and the comparable brightness temperature of the dust and ^{13}CO emission suggest that the grains have not yet grown beyond ~ 1 mm and settled to the midplane.

- Although the disk is viewed nearly edge-on, there is evidence of misalignment between different components as the continuum asymmetry along the minor axis (on scales of $\lesssim 0''.05$) and the large-scale outflow ($\sim 100''$) suggest that the east side of the system is the far side, while the SiO jet ($\lesssim 0''.1$) and envelope emission (a few arcsec) suggest that the west side is the far side.
- Different molecules trace different components of the protostellar system. Outflowing material is most clearly visible in ^{12}CO , but also in ^{13}CO , C^{18}O and H_2CO , while SiO traces a compact jet in the western outflow cavity. The outflow cavity wall is also visible in SO. Super-Keplerian ^{12}CO emission in the inner $\sim 1''$ may trace a disk wind. $\text{c-C}_3\text{H}_2$ and DCN only show emission from the envelope, although higher sensitivity is required to rule out their presence in the disk. ^{13}CO , C^{18}O , H_2CO and SO trace the disk and inner envelope, with H_2CO emission arising predominantly in the disk surface layers. SO emission is dominated by the envelope surface along the outflow cavity wall and the disk component originates in the surface layers. This suggests that SO may be tracing UV irradiated regions.
- Analysis of the pv-diagrams of ^{13}CO and C^{18}O results in a ~ 100 au Keplerian rotating disk around a $\sim 0.5 M_\odot$ star.
- The disk is warm, with temperatures of 20–40 K throughout the midplane and $\gtrsim 50$ –60 K in the surface layers. The disk is therefore too warm for CO freeze out, which occurs at a midplane radius of ~ 350 au in the envelope, while H_2CO is frozen out in the midplane down to $\lesssim 25$ au.
- The ^{13}CO brightness temperature and H_2CO line ratio suggest a potential temperature increase around the disk–envelope interface. However, this increase is only seen at redshifted velocities for ^{13}CO and more detailed modeling is required to determine whether the higher temperature occurs in the outer disk or inner envelope, and whether it is associated with an accretion shock.

High resolution observations of multi-wavelength continuum and multiple molecular species are required to

study young disks. Given the complex nature of molecular line emission from a disk–envelope system, these observations need to be combined with source-specific radiative transfer modeling to provide a detailed picture of the physical and chemical structure. The eDisk observations and the work presented here highlight the potential of such studies, and a comparison between the ALMA and JWST NIRC*am* images already shows the synergy between the two observatories.

ACKNOWLEDGMENTS

We thank the referee for carefully reading the manuscript. This paper makes use of the following ALMA data: ADS/JAO.ALMA#2019.1.00261.L, ADS/JAO.ALMA#2019.A.00034.S and

ADS/JAO.ALMA#2017.1.00509.S. ALMA is a partnership of ESO (representing its member states), NSF (USA) and NINS (Japan), together with NRC (Canada), MOST and ASIAA (Taiwan), and KASI (Republic of Korea), in cooperation with the Republic of Chile. The Joint ALMA Observatory is operated by ESO, AUI/NRAO and NAOJ. The National Radio Astronomy Observatory is a facility of the National Science Foundation operated under cooperative agreement by Associated Universities, Inc. M.L.R.H acknowledges support from the Michigan Society of Fellows. J.J.T. acknowledges support from NASA XRP 80NSSC22K1159. Z.-Y.L. is supported in part by NASA NSSC20K0533 and NSF AST-1910106. N.O. acknowledges support from National Science and Technology Council (NSTC) in Taiwan through the grants NSTC 109-2112-M-001-051 and 110-2112-M-001-031. J.K.J., S.G., and R.S. acknowledge support from the Independent Research Fund Denmark (grant No. 0135-00123B). Z.-Y.D.L. acknowledges support from NASA 80NSSC18K1095, the Jefferson Scholars Foundation, the NRAO ALMA Student Observing Support (SOS) SOSPA8-003, the Achievements Rewards for College Scientists (ARCS) Foundation Washington Chapter, the Virginia Space Grant Consortium (VSGC), and UVA research computing (RIVANNA). Y.A. acknowledges support by NAOJ ALMA Scientific Research Grant code 2019-13B, Grant-in-Aid for Scientific Research (S) 18H05222, and Grant-in-Aid for Transformative Research Areas (A) 20H05844 and 20H05847. I.d.G. acknowledges support from grant PID2020-114461GB-I00, funded by MCIN/AEI/10.13039/501100011033. P.M.K. acknowledges support from NSTC 108-2112-M-001-012, NSTC 109-2112-M-001-022 and NSTC 110-2112-M-001-057. W.K. was supported by the National Research Foundation of Korea (NRF) grant funded by the

Korea government (MSIT) (NRF-2021R1F1A1061794). C.W.L. is supported by the Basic Science Research Program through the National Research Foundation of Korea (NRF) funded by the Ministry of Education, Science and Technology (NRF- 2019R1A2C1010851), and by the Korea Astronomy and Space Science Institute grant funded by the Korea government (MSIT; Project No. 2022-1-840-05). J.E.L. was supported by the National Research Foundation of Korea (NRF) grant funded by the Korean government (MSIT) (grant number 2021R1A2C1011718). L.W.L. acknowledges support from NSF AST-2108794. S.N. acknowledges support from the National Science Foundation through the Graduate Research Fellowship Program under Grant No. 2236415. Any opinions, findings, and conclu-

sions or recommendations expressed in this material are those of the authors and do not necessarily reflect the views of the National Science Foundation. S.T. is supported by JSPS KAKENHI Grant Numbers 21H00048 and 21H04495. This work was supported by NAOJ ALMA Scientific Research Grant Code 2022-20A. S.P.L. and T.J.T. acknowledge grants from the National Science and Technology Council of Taiwan 106-2119-M-007-021-MY3 and 109-2112-M-007-010-MY3. J.P.W. acknowledges support from NSF AST-2107841. H.-W.Y. acknowledges support from the National Science and Technology Council (NSTC) in Taiwan through the grant NSTC 110-2628-M-001-003-MY3 and from the Academia Sinica Career Development Award (AS-CDA-111-M03).

REFERENCES

- Aikawa, Y., van Zadelhoff, G. J., van Dishoeck, E. F., & Herbst, E. 2002, *A&A*, 386, 622, doi: [10.1051/0004-6361:20020037](https://doi.org/10.1051/0004-6361:20020037)
- ALMA Partnership, Brogan, C. L., Pérez, L. M., et al. 2015, *ApJL*, 808, L3, doi: [10.1088/2041-8205/808/1/L3](https://doi.org/10.1088/2041-8205/808/1/L3)
- Ansdell, M., Williams, J. P., van der Marel, N., et al. 2016, *ApJ*, 828, 46, doi: [10.3847/0004-637X/828/1/46](https://doi.org/10.3847/0004-637X/828/1/46)
- Aota, T., Inoue, T., & Aikawa, Y. 2015, *ApJ*, 799, 141, doi: [10.1088/0004-637X/799/2/141](https://doi.org/10.1088/0004-637X/799/2/141)
- Arce, H. G., Shepherd, D., Gueth, F., et al. 2007, in *Protostars and Planets V*, ed. B. Reipurth, D. Jewitt, & K. Keil, 245. <https://arxiv.org/abs/astro-ph/0603071>
- Aso, Y., & Machida, M. N. 2020, *ApJ*, 905, 174, doi: [10.3847/1538-4357/abc6fc](https://doi.org/10.3847/1538-4357/abc6fc)
- Aso, Y., Ohashi, N., Saigo, K., et al. 2015, *ApJ*, 812, 27, doi: [10.1088/0004-637X/812/1/27](https://doi.org/10.1088/0004-637X/812/1/27)
- Aso, Y., Ohashi, N., Aikawa, Y., et al. 2017, *ApJ*, 849, 56, doi: [10.3847/1538-4357/aa8264](https://doi.org/10.3847/1538-4357/aa8264)
- Beckwith, S. V. W., Sargent, A. I., Chini, R. S., & Guesten, R. 1990, *AJ*, 99, 924, doi: [10.1086/115385](https://doi.org/10.1086/115385)
- Bergin, E. A., Du, F., Cleaves, L. I., et al. 2016, *ApJ*, 831, 101, doi: [10.3847/0004-637X/831/1/101](https://doi.org/10.3847/0004-637X/831/1/101)
- Birnsteel, T., Dullemond, C. P., Zhu, Z., et al. 2018, *ApJL*, 869, L45, doi: [10.3847/2041-8213/aaf743](https://doi.org/10.3847/2041-8213/aaf743)
- Brinch, C., & Hogerheijde, M. R. 2010, *A&A*, 523, A25, doi: [10.1051/0004-6361/201015333](https://doi.org/10.1051/0004-6361/201015333)
- Bryden, G., Chen, X., Lin, D. N. C., Nelson, R. P., & Papaloizou, J. C. B. 1999, *ApJ*, 514, 344, doi: [10.1086/306917](https://doi.org/10.1086/306917)
- Caselli, P., Benson, P. J., Myers, P. C., & Tafalla, M. 2002, *ApJ*, 572, 238, doi: [10.1086/340195](https://doi.org/10.1086/340195)
- Cassen, P., & Moosman, A. 1981, *Icarus*, 48, 353, doi: [10.1016/0019-1035\(81\)90051-8](https://doi.org/10.1016/0019-1035(81)90051-8)
- Cook, B. T., Tobin, J. J., Skrutskie, M. F., & Nelson, M. J. 2019, *A&A*, 626, A51, doi: [10.1051/0004-6361/201935419](https://doi.org/10.1051/0004-6361/201935419)
- Dong, R., Liu, S.-y., Eisner, J., et al. 2018, *ApJ*, 860, 124, doi: [10.3847/1538-4357/aac6cb](https://doi.org/10.3847/1538-4357/aac6cb)
- Fedoseev, G., Cuppen, H. M., Ioppolo, S., Lamberts, T., & Linnartz, H. 2015, *MNRAS*, 448, 1288, doi: [10.1093/mnras/stu2603](https://doi.org/10.1093/mnras/stu2603)
- Flores-Rivera, L., Terebey, S., Willacy, K., et al. 2021, *ApJ*, 908, 108, doi: [10.3847/1538-4357/abd1db](https://doi.org/10.3847/1538-4357/abd1db)
- Foreman-Mackey, D., Hogg, D. W., Lang, D., & Goodman, J. 2013, *PASP*, 125, 306, doi: [10.1086/670067](https://doi.org/10.1086/670067)
- Galli, P. A. B., Loinard, L., Bouy, H., et al. 2019, *A&A*, 630, A137, doi: [10.1051/0004-6361/201935928](https://doi.org/10.1051/0004-6361/201935928)
- Garrod, R. T., & Herbst, E. 2006, *A&A*, 457, 927, doi: [10.1051/0004-6361:20065560](https://doi.org/10.1051/0004-6361:20065560)
- Guzmán, V. V., Pety, J., Goicoechea, J. R., et al. 2015, *ApJL*, 800, L33, doi: [10.1088/2041-8205/800/2/L33](https://doi.org/10.1088/2041-8205/800/2/L33)
- Harsono, D., Bjerkele, P., van der Wiel, M. H. D., et al. 2018, *Nature Astronomy*, 2, 646, doi: [10.1038/s41550-018-0497-x](https://doi.org/10.1038/s41550-018-0497-x)
- Harsono, D., van der Wiel, M. H. D., Bjerkele, P., et al. 2021, *A&A*, 646, A72, doi: [10.1051/0004-6361/202038697](https://doi.org/10.1051/0004-6361/202038697)
- Hasegawa, T. I., & Herbst, E. 1993, *MNRAS*, 263, 589, doi: [10.1093/mnras/263.3.589](https://doi.org/10.1093/mnras/263.3.589)
- Hogerheijde, M. R., van Dishoeck, E. F., Blake, G. A., & van Langevelde, H. J. 1998, *ApJ*, 502, 315, doi: [10.1086/305885](https://doi.org/10.1086/305885)
- Jones, D. C., Lam, K. H., Li, Z.-Y., & Tu, Y. 2022, *MNRAS*, 517, 213, doi: [10.1093/mnras/stac1842](https://doi.org/10.1093/mnras/stac1842)
- Kataoka, A., Muto, T., Momose, M., Tsukagoshi, T., & Dullemond, C. P. 2016, *ApJ*, 820, 54, doi: [10.3847/0004-637X/820/1/54](https://doi.org/10.3847/0004-637X/820/1/54)

- Kataoka, A., Muto, T., Momose, M., et al. 2015, *ApJ*, 809, 78, doi: [10.1088/0004-637X/809/1/78](https://doi.org/10.1088/0004-637X/809/1/78)
- Kenyon, S. J., Dobrzycka, D., & Hartmann, L. 1994, *AJ*, 108, 1872, doi: [10.1086/117200](https://doi.org/10.1086/117200)
- Kwon, W., Looney, L. W., Mundy, L. G., Chiang, H.-F., & Kembball, A. J. 2009, *ApJ*, 696, 841, doi: [10.1088/0004-637X/696/1/841](https://doi.org/10.1088/0004-637X/696/1/841)
- Lee, C.-F., Mundy, L. G., Reipurth, B., Ostriker, E. C., & Stone, J. M. 2000, *ApJ*, 542, 925, doi: [10.1086/317056](https://doi.org/10.1086/317056)
- Loinard, L., Rodríguez, L. F., D'Alessio, P., Wilner, D. J., & Ho, P. T. P. 2002, *ApJL*, 581, L109, doi: [10.1086/345940](https://doi.org/10.1086/345940)
- Loomis, R. A., Cleeves, L. I., Öberg, K. I., Guzman, V. V., & Andrews, S. M. 2015, *ApJL*, 809, L25, doi: [10.1088/2041-8205/809/2/L25](https://doi.org/10.1088/2041-8205/809/2/L25)
- Luhman, K. L. 2018, *AJ*, 156, 271, doi: [10.3847/1538-3881/aae831](https://doi.org/10.3847/1538-3881/aae831)
- Mangum, J. G., & Wootten, A. 1993, *ApJS*, 89, 123, doi: [10.1086/191841](https://doi.org/10.1086/191841)
- Maret, S., Maury, A. J., Belloche, A., et al. 2020, *A&A*, 635, A15, doi: [10.1051/0004-6361/201936798](https://doi.org/10.1051/0004-6361/201936798)
- Miotello, A., Facchini, S., van Dishoeck, E. F., et al. 2019, *A&A*, 631, A69, doi: [10.1051/0004-6361/201935441](https://doi.org/10.1051/0004-6361/201935441)
- Miura, H., Yamamoto, T., Nomura, H., et al. 2017, *ApJ*, 839, 47, doi: [10.3847/1538-4357/aa67df](https://doi.org/10.3847/1538-4357/aa67df)
- Murillo, N. M., van Dishoeck, E. F., van der Wiel, M. H. D., et al. 2018, *A&A*, 617, A120, doi: [10.1051/0004-6361/201731724](https://doi.org/10.1051/0004-6361/201731724)
- Nakatani, R., Liu, H. B., Ohashi, S., et al. 2020, *ApJL*, 895, L2, doi: [10.3847/2041-8213/ab8eaa](https://doi.org/10.3847/2041-8213/ab8eaa)
- Noble, J. A., Theule, P., Mispelaer, F., et al. 2012, *A&A*, 543, A5, doi: [10.1051/0004-6361/201219437](https://doi.org/10.1051/0004-6361/201219437)
- Öberg, K. I., Guzmán, V. V., Merchantz, C. J., et al. 2017, *ApJ*, 839, 43, doi: [10.3847/1538-4357/aa689a](https://doi.org/10.3847/1538-4357/aa689a)
- Ohashi, N., Hayashi, M., Ho, P. T. P., & Momose, M. 1997, *ApJ*, 475, 211, doi: [10.1086/303533](https://doi.org/10.1086/303533)
- Ohashi, N., Jørgensen, J., Tobin, J., & eDisk team. 2022a, *ApJ*
- Ohashi, N., Saigo, K., Aso, Y., et al. 2014, *ApJ*, 796, 131, doi: [10.1088/0004-637X/796/2/131](https://doi.org/10.1088/0004-637X/796/2/131)
- Ohashi, S., Nakatani, R., Liu, H. B., et al. 2022b, *ApJ*, 934, 163, doi: [10.3847/1538-4357/ac794e](https://doi.org/10.3847/1538-4357/ac794e)
- Okoda, Y., Oya, Y., Sakai, N., et al. 2018, *ApJL*, 864, L25, doi: [10.3847/2041-8213/aad8ba](https://doi.org/10.3847/2041-8213/aad8ba)
- Oya, Y., Sakai, N., Lefloch, B., et al. 2015, *ApJ*, 812, 59, doi: [10.1088/0004-637X/812/1/59](https://doi.org/10.1088/0004-637X/812/1/59)
- Oya, Y., Sakai, N., López-Sepulcre, A., et al. 2016, *ApJ*, 824, 88, doi: [10.3847/0004-637X/824/2/88](https://doi.org/10.3847/0004-637X/824/2/88)
- Oya, Y., Moriwaki, K., Onishi, S., et al. 2018, *ApJ*, 854, 96, doi: [10.3847/1538-4357/aaa6c7](https://doi.org/10.3847/1538-4357/aaa6c7)
- Podio, L., Garufi, A., Codella, C., et al. 2020, *A&A*, 642, L7, doi: [10.1051/0004-6361/202038952](https://doi.org/10.1051/0004-6361/202038952)
- Reipurth, B., Rodríguez, L. F., Anglada, G., & Bally, J. 2004, *AJ*, 127, 1736, doi: [10.1086/381062](https://doi.org/10.1086/381062)
- Roccatagliata, V., Franciosini, E., Sacco, G. G., Randich, S., & Sicilia-Aguilar, A. 2020, *A&A*, 638, A85, doi: [10.1051/0004-6361/201936401](https://doi.org/10.1051/0004-6361/201936401)
- Rosenfeld, K. A., Andrews, S. M., Hughes, A. M., Wilner, D. J., & Qi, C. 2013, *ApJ*, 774, 16, doi: [10.1088/0004-637X/774/1/16](https://doi.org/10.1088/0004-637X/774/1/16)
- Sai, J., Ohashi, N., Saigo, K., et al. 2020, *ApJ*, 893, 51, doi: [10.3847/1538-4357/ab8065](https://doi.org/10.3847/1538-4357/ab8065)
- Sakai, N., Hanawa, T., Zhang, Y., et al. 2019, *Nature*, 565, 206, doi: [10.1038/s41586-018-0819-2](https://doi.org/10.1038/s41586-018-0819-2)
- Sakai, N., Oya, Y., Sakai, T., et al. 2014a, *ApJL*, 791, L38, doi: [10.1088/2041-8205/791/2/L38](https://doi.org/10.1088/2041-8205/791/2/L38)
- Sakai, N., Sakai, T., Hirota, T., et al. 2014b, *Nature*, 507, 78, doi: [10.1038/nature13000](https://doi.org/10.1038/nature13000)
- Sakai, N., Oya, Y., Higuchi, A. E., et al. 2017, *MNRAS*, 467, L76, doi: [10.1093/mnras/slx002](https://doi.org/10.1093/mnras/slx002)
- Segura-Cox, D. M., Schmiedeke, A., Pineda, J. E., et al. 2020, *Nature*, 586, 228, doi: [10.1038/s41586-020-2779-6](https://doi.org/10.1038/s41586-020-2779-6)
- Seifried, D., Sánchez-Monge, Á., Walch, S., & Banerjee, R. 2016, *MNRAS*, 459, 1892, doi: [10.1093/mnras/stw785](https://doi.org/10.1093/mnras/stw785)
- Shariff, K., Gorti, U., & Melon Fuksman, J. D. 2022, *MNRAS*, 514, 5548, doi: [10.1093/mnras/stac1186](https://doi.org/10.1093/mnras/stac1186)
- Sheehan, P. D., Tobin, J. J., Federman, S., Megeath, S. T., & Looney, L. W. 2020, *ApJ*, 902, 141, doi: [10.3847/1538-4357/abbad5](https://doi.org/10.3847/1538-4357/abbad5)
- Sheehan, P. D., Tobin, J. J., Li, Z.-Y., et al. 2022, *ApJ*, 934, 95, doi: [10.3847/1538-4357/ac7a3b](https://doi.org/10.3847/1538-4357/ac7a3b)
- Shirley, Y. L., Mason, B. S., Mangum, J. G., et al. 2011, *AJ*, 141, 39, doi: [10.1088/0004-6256/141/2/39](https://doi.org/10.1088/0004-6256/141/2/39)
- Tamura, M., Ohashi, N., Hirano, N., Itoh, Y., & Moriarty-Schieven, G. H. 1996, *AJ*, 112, 2076, doi: [10.1086/118164](https://doi.org/10.1086/118164)
- Teague, R., & Foreman-Mackey, D. 2018, *Research Notes of the American Astronomical Society*, 2, 173, doi: [10.3847/2515-5172/aae265](https://doi.org/10.3847/2515-5172/aae265)
- Terwisscha van Scheltinga, J., Hogerheijde, M. R., Cleeves, L. I., et al. 2021, *ApJ*, 906, 111, doi: [10.3847/1538-4357/abc9ba](https://doi.org/10.3847/1538-4357/abc9ba)
- Tobin, J. J., Hartmann, L., Calvet, N., & D'Alessio, P. 2008, *ApJ*, 679, 1364, doi: [10.1086/587683](https://doi.org/10.1086/587683)
- Tobin, J. J., Hartmann, L., Chiang, H.-F., et al. 2012, *Nature*, 492, 83, doi: [10.1038/nature11610](https://doi.org/10.1038/nature11610)
- . 2013, *ApJ*, 771, 48, doi: [10.1088/0004-637X/771/1/48](https://doi.org/10.1088/0004-637X/771/1/48)
- Tobin, J. J., Hartmann, L., Looney, L. W., & Chiang, H.-F. 2010, *ApJ*, 712, 1010, doi: [10.1088/0004-637X/712/2/1010](https://doi.org/10.1088/0004-637X/712/2/1010)

- Tobin, J. J., Hartmann, L., Chiang, H.-F., et al. 2011, *ApJ*, 740, 45, doi: [10.1088/0004-637X/740/1/45](https://doi.org/10.1088/0004-637X/740/1/45)
- Tobin, J. J., Sheehan, P. D., Megeath, S. T., et al. 2020, *ApJ*, 890, 130, doi: [10.3847/1538-4357/ab6f64](https://doi.org/10.3847/1538-4357/ab6f64)
- Tychoniec, L., Manara, C. F., Rosotti, G. P., et al. 2020, *A&A*, 640, A19, doi: [10.1051/0004-6361/202037851](https://doi.org/10.1051/0004-6361/202037851)
- Tychoniec, L., van Dishoeck, E. F., van't Hoff, M. L. R., et al. 2021, *A&A*, 655, A65, doi: [10.1051/0004-6361/202140692](https://doi.org/10.1051/0004-6361/202140692)
- Ulrich, R. K. 1976, *ApJ*, 210, 377, doi: [10.1086/154840](https://doi.org/10.1086/154840)
- van der Wiel, M. H. D., van der Tak, F. F. S., Ossenkopf, V., et al. 2009, *A&A*, 498, 161, doi: [10.1051/0004-6361/200811391](https://doi.org/10.1051/0004-6361/200811391)
- van Gelder, M. L., Tabone, B., van Dishoeck, E. F., & Godard, B. 2021, *A&A*, 653, A159, doi: [10.1051/0004-6361/202141591](https://doi.org/10.1051/0004-6361/202141591)
- van 't Hoff, M. L. R., Tobin, J. J., Harsono, D., & van Dishoeck, E. F. 2018, *A&A*, 615, A83, doi: [10.1051/0004-6361/201732313](https://doi.org/10.1051/0004-6361/201732313)
- van 't Hoff, M. L. R., Harsono, D., Tobin, J. J., et al. 2020, *ApJ*, 901, 166, doi: [10.3847/1538-4357/abb1a2](https://doi.org/10.3847/1538-4357/abb1a2)
- van 't Hoff, M. L. R., Harsono, D., van Gelder, M. L., et al. 2022, *ApJ*, 924, 5, doi: [10.3847/1538-4357/ac3080](https://doi.org/10.3847/1538-4357/ac3080)
- Velusamy, T., Langer, W. D., & Thompson, T. 2014, *ApJ*, 783, 6, doi: [10.1088/0004-637X/783/1/6](https://doi.org/10.1088/0004-637X/783/1/6)
- Williams, J. P., Cieza, L., Hales, A., et al. 2019, *ApJL*, 875, L9, doi: [10.3847/2041-8213/ab1338](https://doi.org/10.3847/2041-8213/ab1338)
- Wilson, T. L., & Rood, R. 1994, *ARA&A*, 32, 191, doi: [10.1146/annurev.aa.32.090194.001203](https://doi.org/10.1146/annurev.aa.32.090194.001203)
- Yang, H., Li, Z.-Y., Looney, L. W., et al. 2016, *MNRAS*, 460, 4109, doi: [10.1093/mnras/stw1253](https://doi.org/10.1093/mnras/stw1253)
- Yen, H.-W., Takakuwa, S., Ohashi, N., et al. 2014, *ApJ*, 793, 1, doi: [10.1088/0004-637X/793/1/1](https://doi.org/10.1088/0004-637X/793/1/1)
- Zhu, Z., Stone, J. M., Rafikov, R. R., & Bai, X.-n. 2014, *ApJ*, 785, 122, doi: [10.1088/0004-637X/785/2/122](https://doi.org/10.1088/0004-637X/785/2/122)
- Zucker, C., Speagle, J. S., Schlafly, E. F., et al. 2019, *ApJ*, 879, 125, doi: [10.3847/1538-4357/ab2388](https://doi.org/10.3847/1538-4357/ab2388)

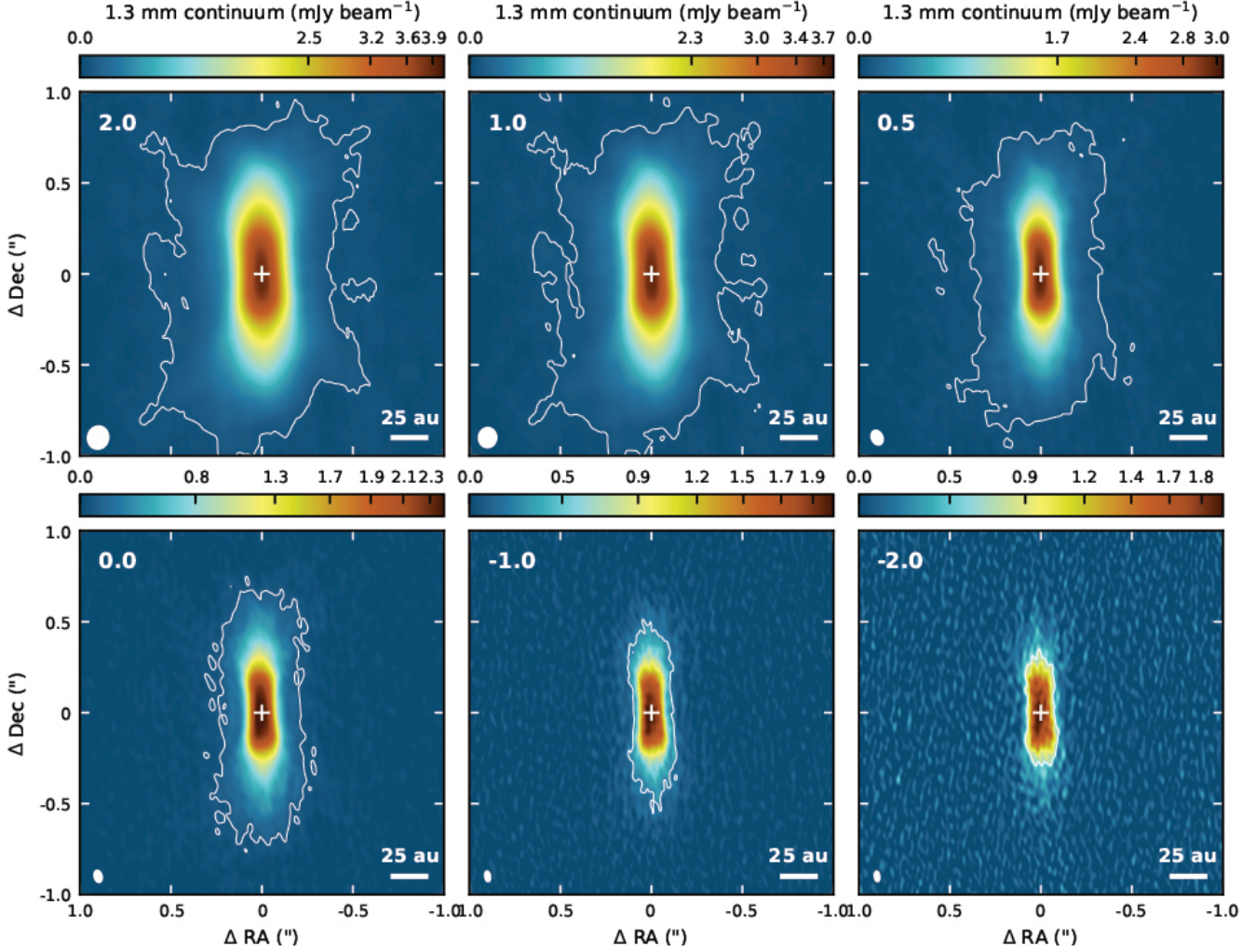


Figure A1. ALMA 1.3 mm continuum image of L1527 imaged with different robust parameters as listed in the top left corner of each panel. The robust = -0.5 image is shown in the left panel of Fig. 2. The beam size is depicted by the white ellipse in the bottom left corner of each panel. The solid white contour marks the 5σ level and the white cross indicates the source position.

APPENDIX

A. ADDITIONAL CONTINUUM IMAGES

Figure A1 presents an overview of the 1.3 mm continuum toward L1527 imaged with different robust parameters in addition to the image made with a robust value of -0.5 as presented in Fig. 2 (left panel). In addition, Fig. A2 presents a similar image for the 3.3 mm continuum image from archival ALMA data (2017.1.00509.S, PI: N. Sakai) as shown in Fig. 2 for 1.3 mm.

B. ADDITIONAL MOLECULAR LINE IMAGES

The individual ^{12}CO , ^{13}CO , and C^{18}O channel maps used to make the RGB overlay (Fig. 5) are shown in Fig. B1. In addition, Figs. B2–B4 present ^{12}CO , ^{13}CO , and C^{18}O channel maps to highlight the outflowing material visible in the three CO isotopologues. Velocity channel maps for the $\text{c-C}_3\text{H}_2$ transitions are displayed in Fig. B5, for DCN in Fig. B6, for $\text{H}_2\text{CO } 3_{2,1} - 2_{2,0}$ in Fig. B7, and for SO in Fig. B8. Figure B9 shows the SO moment eight (peak intensity) map.

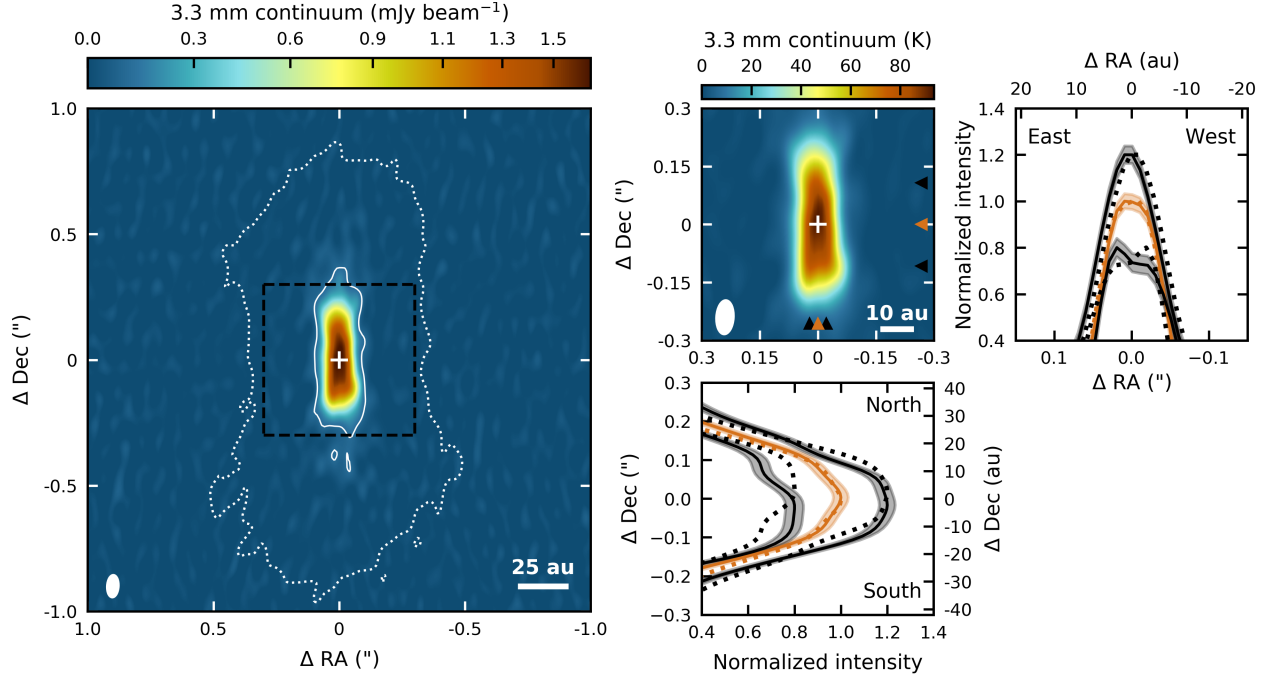


Figure A2. ALMA 3.3 mm continuum image of L1527 from archival data created with the eDisk data reduction script. The left panel shows the full extent of the continuum imaged with a robust parameter of -1.0 (color scale; beam size of $0''.086 \times 0''.043$), with the solid white contour marking the 5σ level ($0.13 \text{ mJy beam}^{-1}$). The dotted white contour marks the 5σ level ($0.04 \text{ mJy beam}^{-1}$) of the map imaged with a robust parameter of 2.0 (beam size of $0''.225 \times 0''.173$). The black dashed square shows the region depicted in the top middle panel, where the brightness temperature of the continuum is displayed. The top right panel shows the normalized intensity along the disk minor axis at source position (orange) and at 15 au to the north (top black curve) and south (bottom black curve). This is a slightly different offset compared to what is shown for the 1.3 mm image, as the asymmetry is strongest at larger radii at 3.3 mm. The bottom right panel shows the normalized intensity along the disk major axis at source position (orange) and at 3 au to the east (left black curve) and west (right black curve). Black and orange triangles in the continuum image (top middle panel) mark the locations of the intensity profiles. The black curves are shifted by 0.2 in normalized intensity with respect to the orange curves for better visibility. The shaded region depicts the 3σ level and the dotted lines are the mirror images of the solid lines to highlight the asymmetries.

C. ADDITIONAL FIGURES

Figure C1 presents the $\text{H}_2\text{CO } 3_{0,3} - 2_{0,2}/3_{2,2} - 2_{2,1}$ line ratio as function of temperature for optically thin emission in LTE.

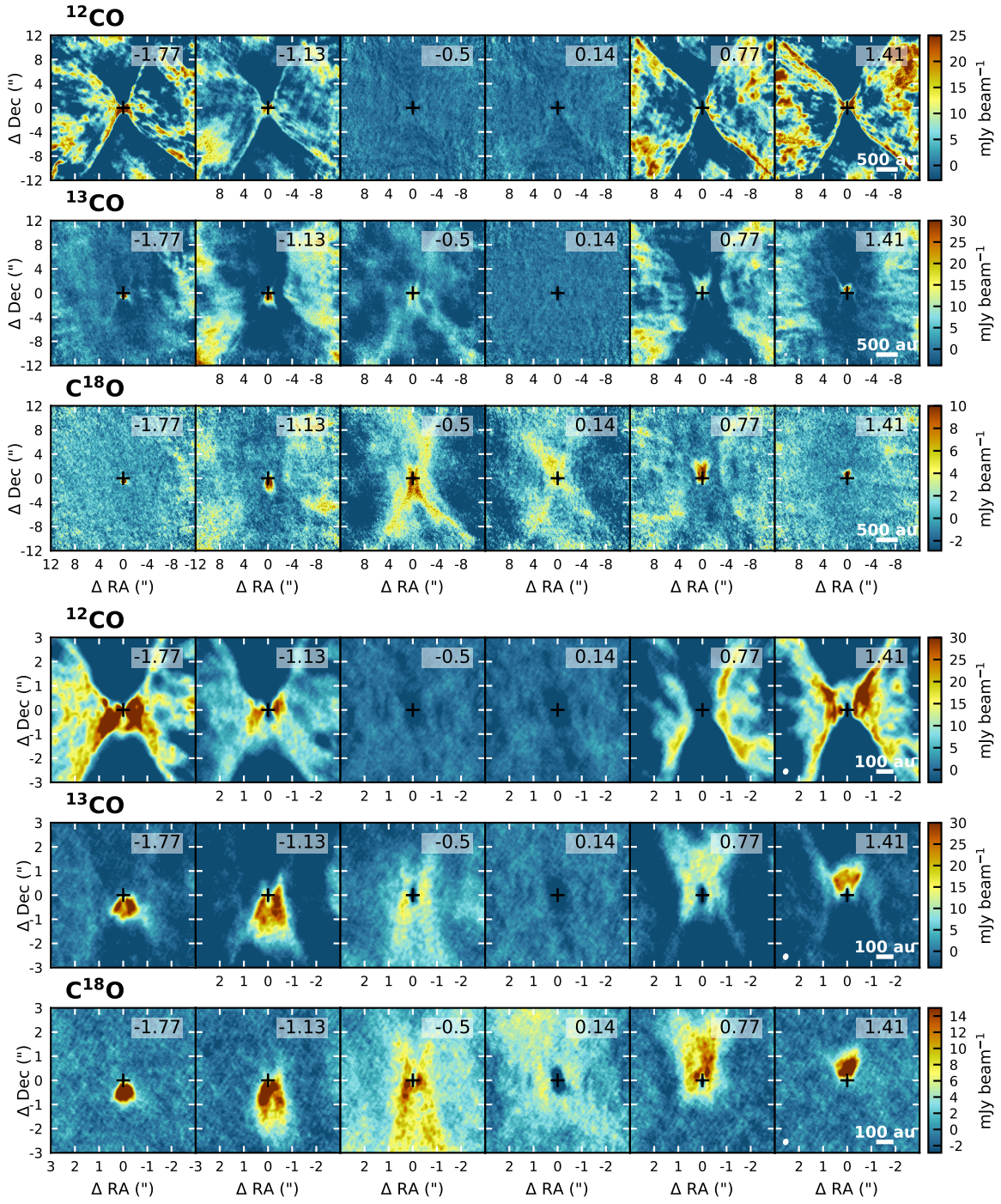


Figure B1. Selected velocity channel maps of ^{12}CO (first and fourth row), ^{13}CO (second and fifth row) and C^{18}O (third and sixth row) as used for the RGB overlay in Fig. 5. The top three rows display the emission on scales of $24''$ (corresponding to the top row in Fig. 5) and the bottom three rows display the emission on scales of $6''$ (corresponding to the bottom row in Fig. 5).

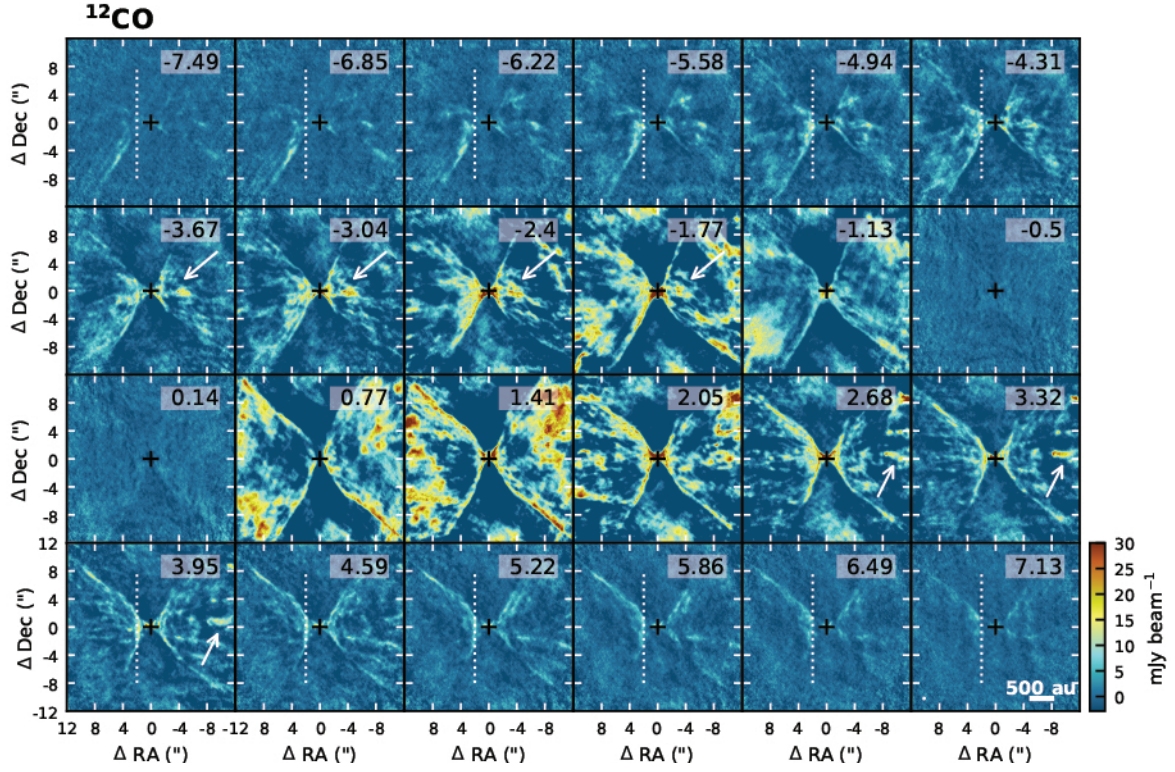


Figure B2. Velocity channel maps of ^{12}CO . The color scale is capped to highlight the large scale emission. A vertical white dotted line is drawn at the same position in the top and bottom panels to guide the eye with respect to the outward moving emission front at the highest velocity offsets. The white arrows at $-3.67 - -1.77 \text{ km s}^{-1}$ and $2.68 - 3.95 \text{ km s}^{-1}$ highlight the potential jets. The beam is depicted in the bottom left corner of the bottom right panel, and the velocity with respect to the system velocity is listed in the top right corner of each panel.

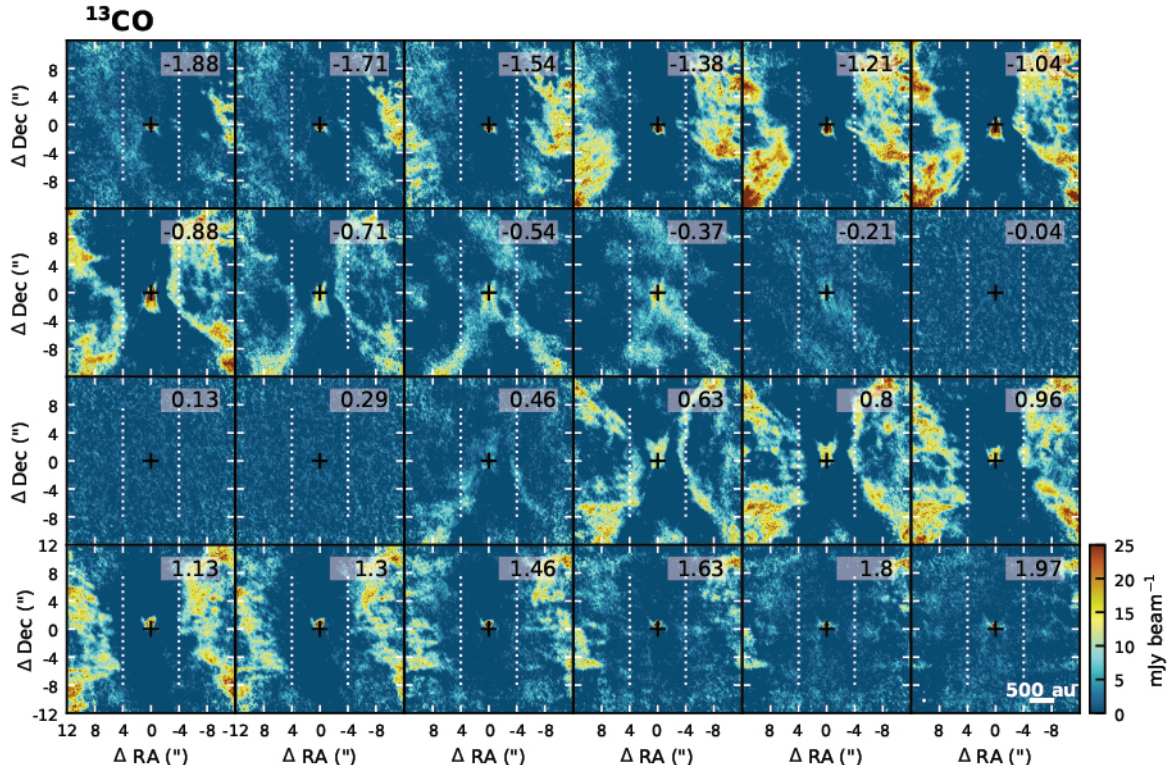


Figure B3. Low and intermediate velocity channel maps of ^{13}CO highlighting the emission in the outflow cavity. Two vertical white dotted lines are drawn at the same position in each panel to guide the eye with respect to the outward moving emission fronts with higher velocity offsets. The beam is depicted in the bottom left corner of the bottom right panel, and the velocity with respect to the system velocity is listed in the top right corner of each panel.

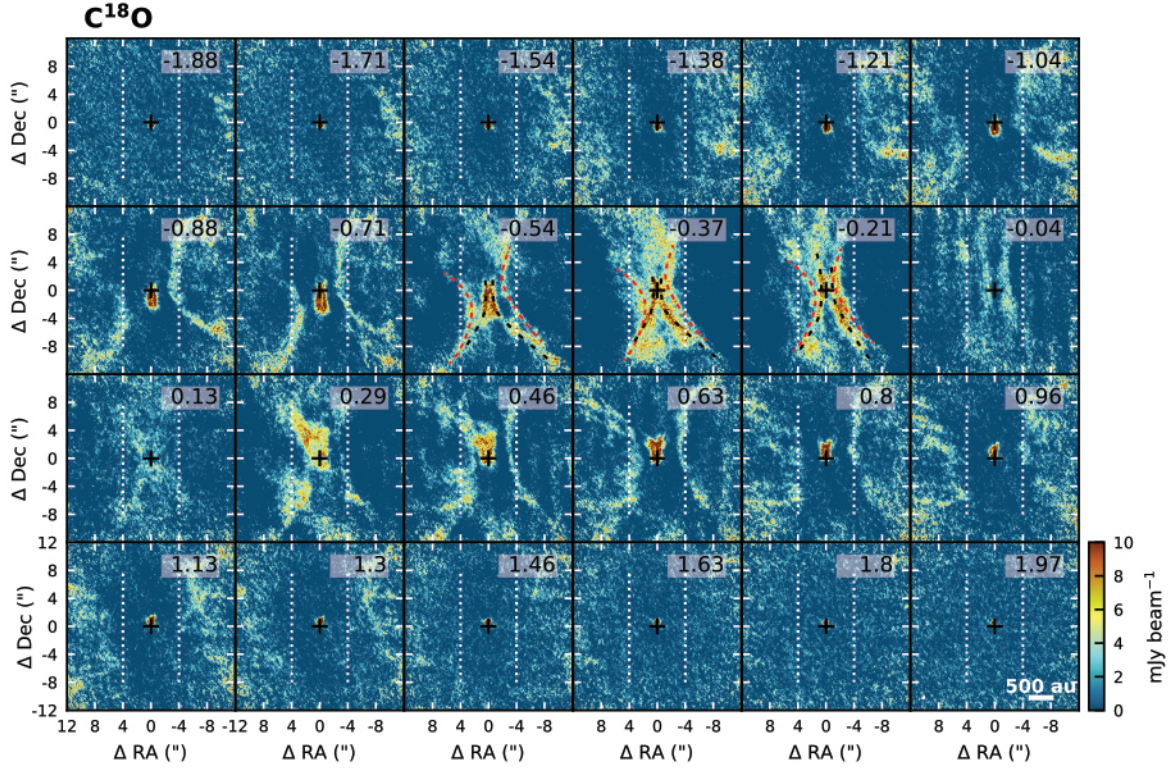


Figure B4. As Fig. B3, but for $C^{18}O$. Different components are outlined in three velocity channels ($-0.54 - -0.21 \text{ km s}^{-1}$), with dashed red lines indicating outflowing material and dashed black lines marking the envelope surface or cavity wall. These curves are drawn by hand and merely serve as a guide for the eyes.

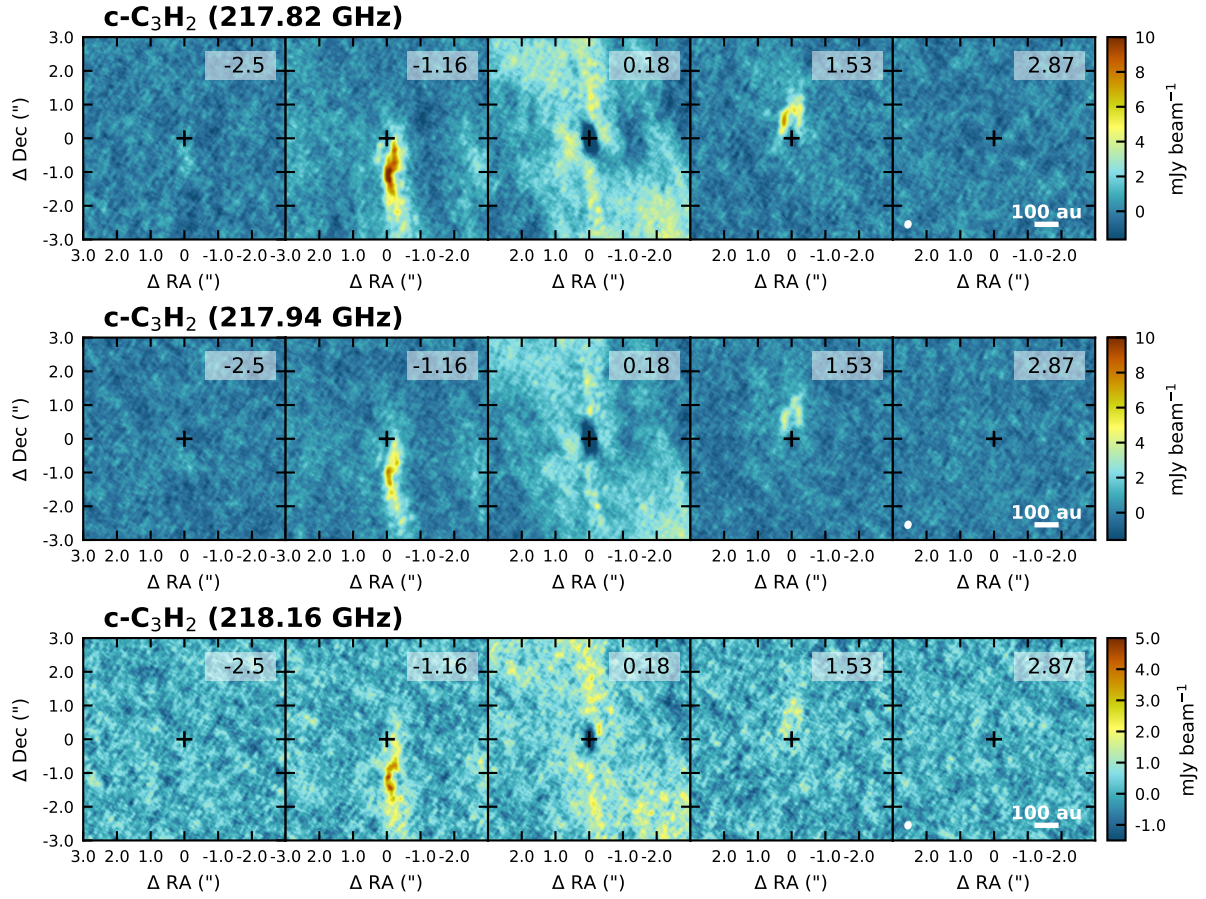


Figure B5. Velocity channel maps of $c\text{-C}_3\text{H}_2$ $6_{0,6} - 5_{1,5}$ blended with $6_{1,6} - 5_{0,5}$ (top row), $5_{1,4} - 4_{2,3}$ (middle row) and $5_{2,4} - 4_{1,3}$ (bottom row).

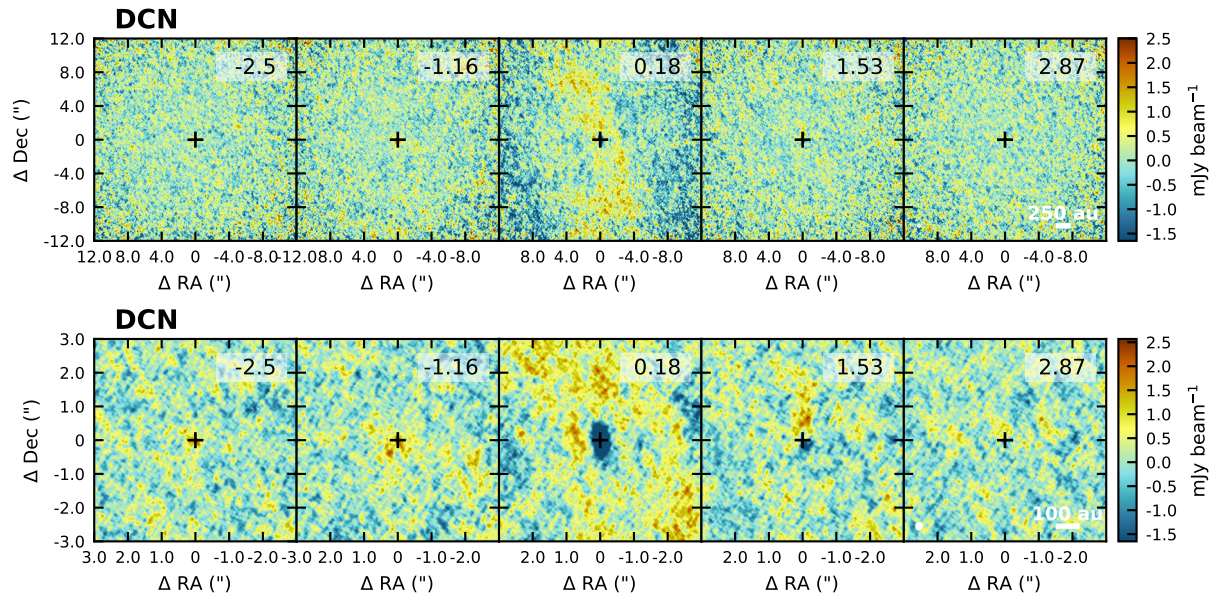


Figure B6. Velocity channel maps of DCN on a $24''$ scale (top row) and $6''$ scale (bottom row).

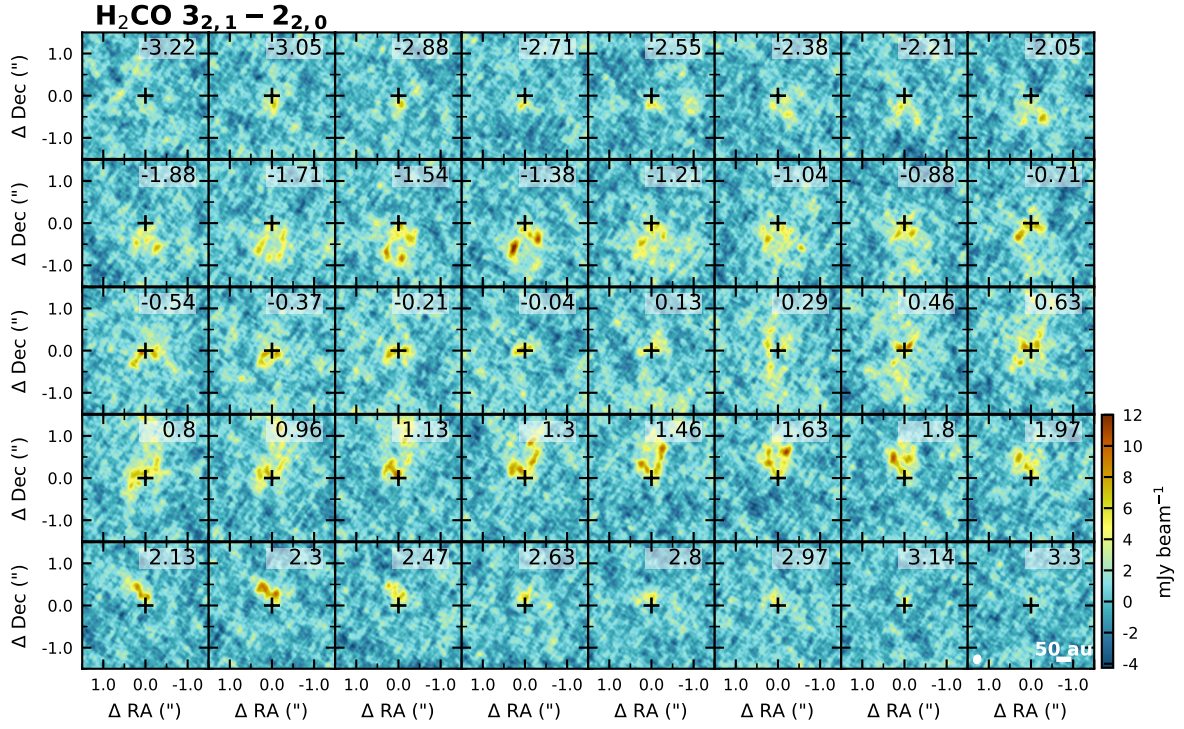


Figure B7. Velocity channel maps of H₂CO 3_{2,1} - 2_{2,0}.

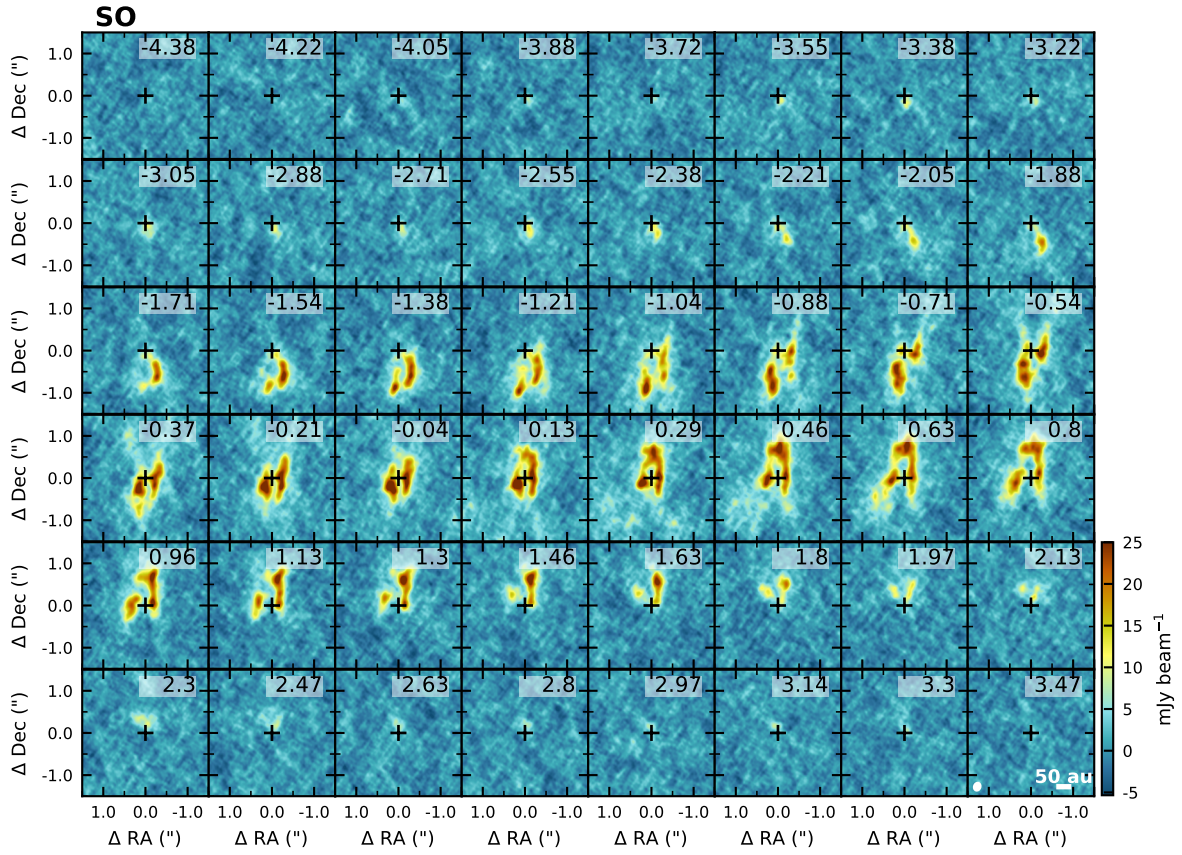


Figure B8. Velocity channel maps of SO

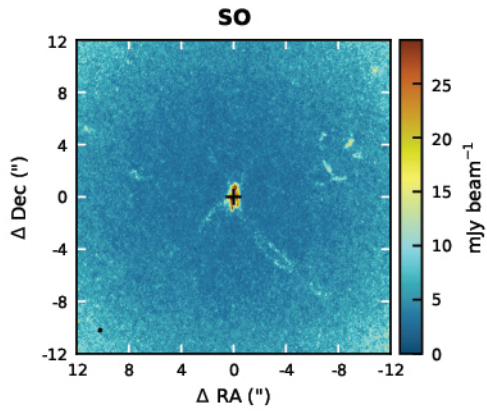


Figure B9. Peak intensity (moment eight) map of SO.

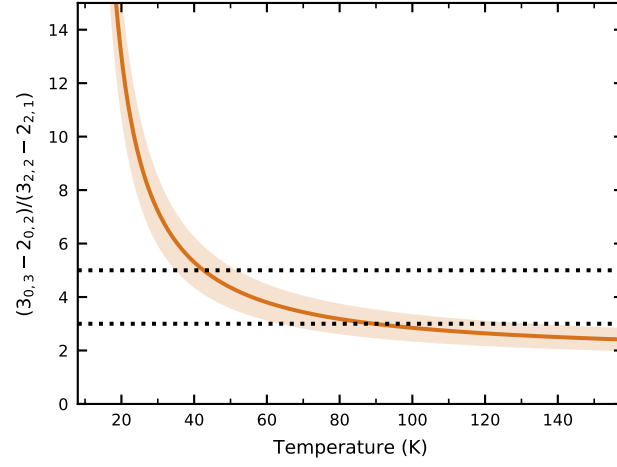


Figure C1. Line ratio of the H₂CO $3_{0,3} - 2_{0,2}$ and $3_{2,2} - 2_{2,1}$ transitions as function of temperature for optically thin emission in LTE. The shaded area marks the uncertainty for a signal-to-noise ratio of 6 for the $3_{2,2} - 2_{2,1}$ transition and 12 for the $3_{0,3} - 2_{0,2}$ transition. Horizontal dotted lines marking line ratios of 3 and 5 are drawn for reference.